Plasmon oscillations in two-dimensional arrays of ultranarrow graphene nanoribbons

A. Sindona [1,2,*] M. Pisarra [3,4] S. Bellucci [5] T. Tene,[6] M. Guevara,[7] and C. Vacacela Gomez[8]

[1]*Dipartimento di Fisica, Università della Calabria, Via P. Bucci, Cubo 30C, I-87036 Rende (CS), Italy*
[2]*INFN-Gruppo Collegato di Cosenza, Cubo 31C, I-87036 Rende (CS), Italy*
[3]*IMDEA Nanociencia, Calle Faraday 9, Cantoblanco, E-28049 Madrid, Spain*
[4]*Departamento de Química, Universidad Autónoma de Madrid, Calle Francisco Tomás y Valiente 7, E-28049 Madrid, Spain*
[5]*INFN-Laboratori Nazionali di Frascati (LNF), Via E. Fermi 40, I-00044 Frascati (RM), Italy*
[6]*Department of Chemistry and Exact Sciences, Universidad Técnica Particular de Loja, EC-110160 Loja, Ecuador*
[7]*Faculty of Mechanical Engineering, Escuela Superior Politécnica de Chimborazo, EC-060101 Riobamba, Ecuador*
[8]*Yachay Tech University, School of Physical Sciences and Nanotechnology, EC-100119 Urcuquí, Ecuador*

The recent ability to manipulate graphene-like structures at the atomic scale is opening up new challenges in electronics and photonics, with a key focus on the bulk and edges of the systems, which generate peculiar and interfering charge density oscillations, quantized as plasmons. These quasiparticles are here scrutinized in planar periodic distributions (two-dimensional arrays) of parallel and atomically wide graphene nanoribbons. Time-dependent density functional theory is used, with a specifically developed adjustment on the random phase approximation, suitable for two-dimensional materials. Several extrinsic conditions (for doped or gated nanoribbon arrays) are simulated to characterize the propagation and interplay of the bulk and edge plasmons, at far infrared to visible energies, and over a broad range of momentum transfers. The main technological interest is on the bulk mode, which is dominant and propagates undamped, at energies below the band gap of the intrinsic systems. On the other hand, the edge mode is always well defined at energies above the band gap, and highly dependent on the band gap value, though it decays via electron-hole excitations between the first valence and conduction bands. Particular attention is paid to the interaction or overlap region of the two plasmons, explaining its sensitivity to induced Fermi level shifting, transferred momentum, ribbon type, and geometry, with the inclusion of many-body, *GW*-like effects. More importantly, the lower-terahertz behavior of the bulk plasmon is explored, highlighting the limits of available non–*ab initio* approaches, suitable for stripes of graphene being tenths of nanometers wide. Then, an effective model is derived from the *ab initio* framework, which reasonably accounts for the two-plasmon response of the studied, ultranarrow nanoribbon systems, at small momentum transfers. The range of applicability of the same derivation procedure may be extended to more complex nanoribbon heterostructures available for synthesis, which emphasizes the need for an *ab initio* guide to a reliable design of nanoplasmonic devices.

I. INTRODUCTION

The quantized, collective oscillations of the valence electron density, at the interface between a low-dimensional nanoscale structure and a dielectric medium, e.g., the vacuum, result in plasmon quasiparticles, which make formidable tools to confine and manipulate the electromagnetic energy at the nanometer scale [1,2].

Soon after its discovery [3,4], graphene emerged as a building block for plasmonic applications [5–8] in a wide spectral range, from the microwave to the visible, because of its intrinsic two-dimensional (2D) and flexible structure [9], excellent electronic transport [10], and unique optical properties [11].

Nowadays, experimental and theoretical studies are oriented to detect, launch, control, and manipulate plasmons in a variety of graphene-based or beyond-graphene materials [12,13], which has led to nanodevice architectures [14–17]

offering the potential for confining optical signals, beyond the diffraction limit of propagating light [18].

Graphene nanoribbons (GNRs) are notable material prototypes to explore plasmon excitations, because they preserve most of the exceptional properties of graphene, with the additional feature that they are semiconductors and their band gap is geometrically controllable [19]. Besides displaying enhanced electronic properties, these narrow stripes of graphene also support a quasi-one-dimensional (1D) charge carrier confinement [20], which calls for a thorough understanding of their dielectric response.

Previous *ab initio* investigations [21,22], based on time-dependent (TD) density functional theory (DFT), in the random phase approximation (RPA), have demonstrated that, independently of the width and chirality of the ribbons, all GNRs are characterized by two interband plasmons at energies larger than about ∼2 eV, specifically, in the higher-visible to the extreme-ultraviolet range. Such intrinsic oscillations are the counterpart of the π-π and π-σ modes, detected in graphene [23,24].

---
*antonello.sindona@fis.unical.it

On the other hand, at energies below the lower visible spectrum, two other, more remarkable resonant oscillations were noticed, being respectively associated with *intraband* and *interband* electron-hole processes, occurring mostly between the first valence and conduction bands (first VBs and CBs) of the systems. These quasiparticles were interpreted as the momentum-space representations of the charge density oscillations localized in and at the ends of the GNRs, namely *bulk* and *edge* plasmons, consistently reported in a number of experiments [25–29].

Indeed, the (extrinsic, bulk) intraband and (intrinsic, edge) interband modes of several GNRs have been proved to be tunable by changing some specific geometric, physical, or chemical parameters, such as the unit cell bond lengths, angles, or chirality, the charge carrier concentration or Fermi level (doping), and the incident momentum or inclination relative to the ribbon (longitudinal) axis. Nonetheless, a systematic analysis of the effect of these parameters on the shape and dispersion of the same modes, over the whole infrared domain, with a proper *ab initio* framework, is still lacking.

Here, we provide such a study using a TDDFT+RPA approach at finite temperature ($\gtrsim 100$ K), specifically developed for extrinsic (doped) and intrinsic (undoped) GNRs, in periodic planar array form [21,22]. Our attention is on the ultranarrow 5AGNR and 11AGNR geometries respectively characterized by 5 and 11 carbon dimer lines across the nanoribbon width [30,31], ended by perfectly symmetric hydrogen-passivated edges.

In this regard, we analyze the electronic structure of the systems (Sec. II), with particular reference to the (slightly) asymmetric dispersions of the highest occupied and lowest unoccupied energy bands (first VB and CB), including relaxation effects, many-body band gap corrections, and related semiphenomenological modeling.

Then, we focus on the propagation and interplay between the intraband and interband plasmons (Sec. III), which are the key elements of plasmonic and photonic applications on GNR-based devices. We first consider small to large doping concentrations, at near-infrared to visible energies (below ∼2.0 eV), and incident momenta, of length below ∼0.2 Å^{-1}, parallel or inclined with respect to the GNRs' axis (Sec. IV). In the same context, we specifically deal with the interaction or overlap region of the two plasmons, plus its sensitivity to charge carrier doping or gating, ribbon type, geometry, transferred momentum, and many-body interactions. Next, we present the mid- to far-infrared terahertz (THz) frequency behavior of the intraband plasmon (Sec. V) and compare its dielectric response with some known results based on available *non–ab initio* approaches [32,33], while at the same time highlighting their limits.

Finally, we derive an *ab initio*–guided model (Sec. VI), which provides a sufficiently accurate description of the plasmon behavior of currently synthesized ultranarrow GNRs [34–37], in a limited range of their tunable parameters, and may be extended to more sophisticated nanoribbon structures.

II. BAND STRUCTURE

As is routinely done in TDDFT [38,39], the ground-state one-electron properties of 5AGNR and 11AGNR were
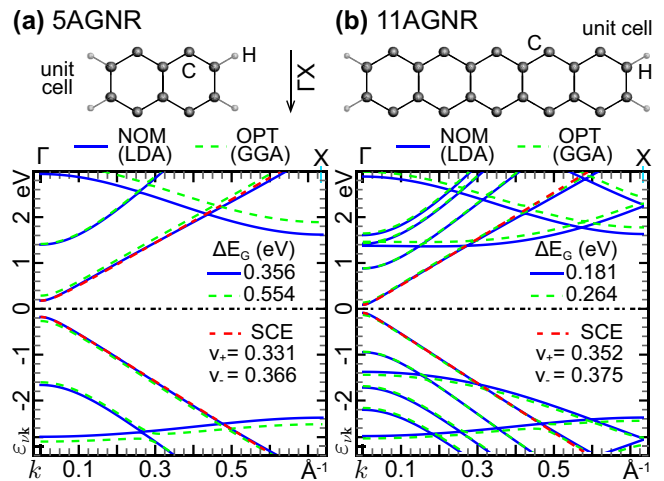

FIG. 1. Structural and electronic properties of 5AGNR (a) and 11AGNR (b), obtained from PW-DFT under the LDA and GGA, respectively, using the nominal (NOM, blue lines) and the geometry-optimized (OPT, dashed green lines) unit cells, detailed in the main text and Appendix B. The energy bands are plotted vs longitudinal wave vectors of the first BZ (along the ΓX segment). The LDA and GGA dispersions are nearly indistinguishable at 1.2–1.5 eV above or below the intrinsic Fermi level E_F (set to zero), with slightly different band gap values ΔE_G. The first valence and conduction bands have clear nonparabolic dispersions, in excellent agreement with the SCE model of Eq. (1), where v_+ and v_- are expressed in units of the Bohr velocity. All bands are flat (i.e., nondispersive) with respect to transverse wave vectors of the first BZ.

determined by plane wave (PW) DFT, within the Kohn-Sham (KS) formalism [40]. Electronic structure calculations were performed at the level of the local density [41] and generalized gradient [42] approximations (LDA and GGA), in conjunction with suitable, norm-conserving pseudopotential schemes [43,44] to eliminate the core electrons (Appendix A).

The three-dimensional (3D) periodicity, inherent in PW-DFT, was implemented by equally spaced distributions of parallel GNR stripes. The main outputs, for subsequent dielectric calculations, were the valence electron wave functions $\{|\nu\mathbf{k}\rangle\}$ and associated energies $\{\varepsilon_{\nu\mathbf{k}}\}$, indexed by the band number ν and the reduced wave vector $\mathbf{k}$ of the first Brillouin zone (first BZ).

Different structural relaxation tests, detailed in Appendix B, indicated that the unit cells of the systems are weakly distorted, by less than 4%, from their ideal or nominal configurations, set by hexagonal stripes with C-C bond lengths of 1.42 Å and C-H bond lengths of 1.09 Å, as sketched in Fig. 1 [and reported in Figs. 20(c) and 21(b) of Appendix B].

Accordingly, we performed DFT-LDA calculations on the ideal GNR geometries, used as reference, in comparison with DFT-GGA calculations on the optimized GNR unit cells (Appendix A 1). The marginal effect of geometry optimization reflects the almost identical dispersions, at a few eV around the intrinsic Fermi energy E_F, of the LDA and GGA bands. These are reported in Fig. 1 (and Fig. 22 of Appendix C) along the irreducible (longitudinal) part of the first BZ, i.e., the ΓX segment, which provides the periodic direction of the

1D GNR element, whose 2D repetition generates the planar array [Fig. 20(b) of Appendix B].

A projected band analysis confirmed that the valence electron wave functions $\langle \mathbf{r} | \nu \mathbf{k} \rangle$, involved in the same energy window, are entirely made of p_z (π, π^*) orbitals, as expected from a *virtual cut* of the graphene electronic structure (Appendix D).

At a closer look, significant differences, on the 0.1 eV scale, occur at the Γ point that particularly affect the band gap ΔE_G of the two GNRs, with the GGA values (~ 0.55 eV for 5AGNR, 0.26 eV for 11AGNR) being generally larger than the LDA values (~ 0.36 eV for 5AGNR, ~ 0.18 eV for 11AGNR), as also reported in Appendix C.

Larger discrepancies on suspended GNRs are predicted by many-body perturbation theory, in the *GW* approximation [31] (~ 1.70 eV for 5ANGR and ~ 0.90 eV for 11AGNR). Indeed, even small changes in ΔE_G, say, of ~ 0.05 eV, may have nontrivial consequences on the interband plasmon and the way it is correlated to the intraband plasmon over the visible band, as will be shown in Sec. IV C.

However, the interaction of several GNRs with specific supporting substrates (SiC) has revealed a notable reduction of the band gap values of the systems, which turn out to be very close to our LDA band gaps [37]. Thus, it makes sense to continue our analysis on the bare LDA electronic structure $\{\varepsilon_{\nu \mathbf{k}}, |\nu \mathbf{k}\rangle\}$, while invoking, in parallel, the scissor operator (SO) approximation [45] to deal with *GW* effects. The DFT-LDA-SO approach consists, then, in splitting the LDA energy spectrum $\{\varepsilon_{\nu \mathbf{k}}\}$ at the Fermi level, in order to replace the LDA band gap with the *GW*-corrected value.

Let us now focus on the first VB ($\nu = -1$) and CB ($\nu = 1$), being the main elements controlling the systems' plasmonics. Figure 1 also shows that these bands are excellently correlated by a nonparabolic dispersion, of the form

$$\varepsilon_{\pm 1 \mathbf{k}} = \pm \sqrt{(\Delta E_G / 2)^2 + \hbar^2 v_\pm^2 k^2}, \tag{1}$$

vs the longitudinal crystal momentum $\hbar k$ of the first BZ (ΓX axis). Equation (1) is provided by the so-called semi-classical electromagnetic (SCE) approach [32,36], with $v_\pm$ denoting the Fermi velocities of the first VB and CB, the latter related to the effective masses $m_\pm$ of the charge carriers by $\Delta E_G = 2 m_\pm v_\pm^2$, with $E_F = 0$. The adjusted values of $v_\pm$ on the LDA bands, reported in Fig. 1, testify to a slight asymmetric behavior of the first VB and CB; see also Sec. VI, Fig. 17. Furthermore, the Fermi velocity difference $|v_+ - v_-|$ decreases with increasing GNR width. We thus expect $v_\pm$ to tend to the Fermi velocities of graphene ($v_- \sim 0.382$, $v_+ \sim 0.377$ in Bohr velocity units with the LDA [46]) as the GNR width tends to infinity; see also Appendix G.

Other non–*ab initio* approaches, relying on the tight-binding (TB) method, are well documented in a large literature; see, e.g., Refs. [12,33,47]. In particular, nearest-neighbor (NN) TB approaches predict all armchair GNRs of the $3p + 2$ family, such as 5AGNR ($p = 1$) and 11AGNR ($p = 3$), to behave as (gapless) semimetals [33]. In this approximation, the VB and CB dispersions are consistent with Eq. (1) at $\Delta E_G = 0$. A band gap opening is recovered by including next-nearest-neighbor terms [47]. Nonetheless, the nearest-neighbor TB band structure of a virtually gapless GNR is

particularly instructive to have a feel of the intraband plasmon features in large-width nanoribbons at THz frequencies.

III. PLASMON SPECTRUM

As a second step of the TDDFT framework, the electronic structure $\{\varepsilon_{\nu \mathbf{k}}, |\nu \mathbf{k}\rangle\}$, computed from the DFT-LDA, DFT-GGA, and DFT-LDA-SO approaches, was plugged into the unperturbed density-density response function [48,49]

$$\chi^0_{\mathbf{GG}'} = \frac{2}{\Omega} \sum_{\mathbf{k}, \nu, \nu'} \frac{(f_{\nu \mathbf{k}} - f_{\nu' \mathbf{k} + \mathbf{q}}) \rho^{\mathbf{kq}}_{\nu\nu'}(\mathbf{G}) \rho^{\mathbf{kq}}_{\nu\nu'}(\mathbf{G}')^*}{\hbar\omega + \varepsilon_{\nu \mathbf{k}} - \varepsilon_{\nu' \mathbf{k} + \mathbf{q}} + i\eta}, \tag{2}$$

triggered by a test particle (electron or photon) of energy $\hbar\omega$ and momentum $\hbar\mathbf{q}$; see also Appendix A 2. Here, the factor of 2 accounts for spin degeneracy. Ω denotes the normalization volume of the electron states $|\nu \mathbf{k}\rangle$ and $|\nu' \mathbf{k} + \mathbf{q}\rangle$, of energies $\varepsilon_{\nu \mathbf{k}}$ and $\varepsilon_{\nu' \mathbf{k} + \mathbf{q}}$, and room-temperature occupation factors $f_{\nu \mathbf{k}}$ and $f_{\nu' \mathbf{k} + \mathbf{q}}$. The same states are associated with the correlation coefficients $\rho^{\mathbf{kq}}_{\nu\nu'}(\mathbf{G}) = \langle \nu \mathbf{k} | e^{-i(\mathbf{G} + \mathbf{q}) \cdot \mathbf{r}} | \nu' \mathbf{k} + \mathbf{q} \rangle$ and $\rho^{\mathbf{kq}}_{\nu\nu'}(\mathbf{G}')^*$, which, in turn, depend on the reciprocal-lattice vectors $\mathbf{G}$ and $\mathbf{G}'$, spanned by the replicated GNR slabs; see Eq. (A3). η is a small damping energy with respect to $\hbar\omega$.

Then, with the $\chi^0_{\mathbf{GG}'}$ matrix at hand, the interacting density-density response function was calculated via the central equation of TDDFT [38]

$$\chi_{\mathbf{GG}'} = \chi^0_{\mathbf{GG}'} + (\chi^0 v \chi)_{\mathbf{GG}'}, \tag{3}$$

where the exchange-correlation part of the v matrix was neglected, approximating it to a local kernel $v_{\mathbf{GG}'}$, specifically designed for 2D systems at the RPA level [21,46,50,51]; see Eq. (A5).

Next, the inverse permittivity matrix was determined as $(\epsilon^{-1})_{\mathbf{GG}'} = \epsilon_0^{-1}(1 + v\chi)_{\mathbf{GG}'}$, with ϵ_0 denoting the vacuum permittivity. Finally, the macroscopic permittivity and loss function were, respectively, obtained as

$$\epsilon^M = \frac{1}{(\epsilon^{-1})_{\mathbf{00}}} \quad \text{and} \quad E_{LOSS} \propto -\text{Im}[(\epsilon^{-1})_{\mathbf{00}}]. \tag{4}$$

The TDDFT-RPA-2D framework just outlined gives access to the dielectric properties of 5GNR and 11AGNR, organized in planar arrays with parallel stripes spaced 20 Å apart, at the DFT level. A genuine plasmon mode is dictated by a double change of sign (a couple of zeros) in the macroscopic real permittivity $\text{Re}(\epsilon^M)$, as function of the probing energy $\hbar\omega$ and for a fixed transferred momentum $\hbar\mathbf{q}$. The lowest in energy of these two zeros is followed by a peak in the absorption spectrum, proportional to the macroscopic imaginary permittivity $\text{Im}(\epsilon^M)$. The highest in energy of the same two zeros is the best approximation to the plasmon resonance energy, occurring in a region where $\text{Im}(\epsilon^M)$ is small and followed by a peak in E_{LOSS}. In addition, a local minimum of $\text{Re}(\epsilon^M)$ may be the signature of a damped plasmon mode, preceded by a maximum in $\text{Im}(\epsilon^M)$ and followed by a peak in E_{LOSS}.

In the following, we will specifically explore the near-infrared to visible ($\hbar\omega \leqslant 2.0$ eV, $q \leqslant 0.15$ Å^{-1}) and mid- to far-infrared ($\hbar\omega \leqslant 50$ THz, $q \leqslant 10^5$ cm^{-1}) ranges (Sec. IV and Sec. V) at room temperature, using E_{LOSS} as a figure of merit for the plasmon structure, i.e., the *plasmon spectrum*.
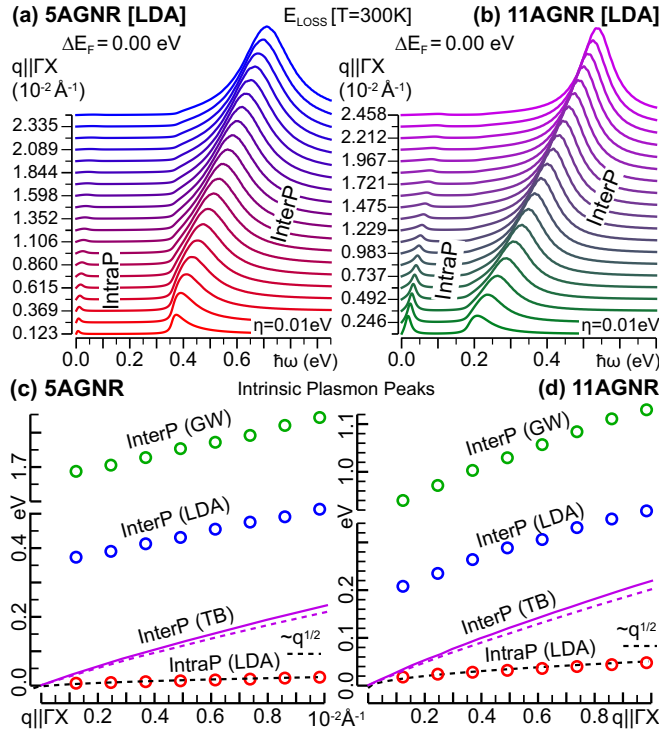
FIG. 2. Intrinsic loss function E_{LOSS} [(a), (b)] and loss peak dispersions [(c), (d)] of 5AGNR [(a), (c)] and 11AGNR [(b), (d)] vs a probing energy $\hbar\omega \leqslant 1.0$ eV. The different plasmon spectra in (a) and (b), acquired at room temperature for some transferred wave vectors $q \leqslant 0.025$ Å^{-1}, parallel to the GNRs' axis ($q\|\Gamma X$), are reported on an arbitrary intensity scale and displaced vertically for clarity. The InterP mode is well separated from, and negligibly overlapping with, a tiny IntraP mode (appreciable only with the small, LDA band gap values). The InterP peaks in (c) and (d) (computed with both the LDA and *GW*-corrected band gaps) are compared with NN p_z-TB calculations [33] (magenta lines), using two different localization parameters for the p_z orbitals. A tiny IntraP mode (computed with the LDA band gaps only) is also detected and reported for $\hbar\omega \leqslant 0.05$ eV, $q \leqslant 0.012$ Å^{-1}.

IV. INTRABAND AND INTERBAND PLASMONS

To begin, let us explore the $\hbar\omega < 4$ eV range with transferred wave vectors of length $q = 0.001$–0.2 Å^{-1}, which was obtained by sampling the $\chi^0_{\mathbf{GG'}}$ matrix of Eq. (2) with an energy resolution of 0.5 meV, and a longitudinal wave vector resolution (inherited from the KS structure of the PW-DFT step) of 1.229×10^{-3} Å^{-1}. The lowest 78 and 54 conduction bands, above 22 and 46 valence bands, were included in the calculation to respectively characterize 5AGNR and 11AGNR. A damping parameter $\eta = 0.01$ eV was adopted to distinguish the loss profiles and plasmon resonances. Different intrinsic and extrinsic conditions were tested, by increasing or decreasing E_F, in the occupation factors $f_{\nu\mathbf{k}}$, $f_{\nu'\mathbf{k+q}}$, entering the $\chi^0_{\mathbf{GG'}}$ matrix of Eq. (2), by an amount ΔE_F. Then, the dielectric properties were computed by plugging $\chi^0_{\mathbf{GG'}}$ into Eqs. (3) and (4). Well converged results were obtained by reducing Eq. (3) to a finite $N_{LF} \times N_{LF}$ matrix equation, including the smallest $N_{LF} \sim 100$ crystal local fields (see also Appendix A 2).
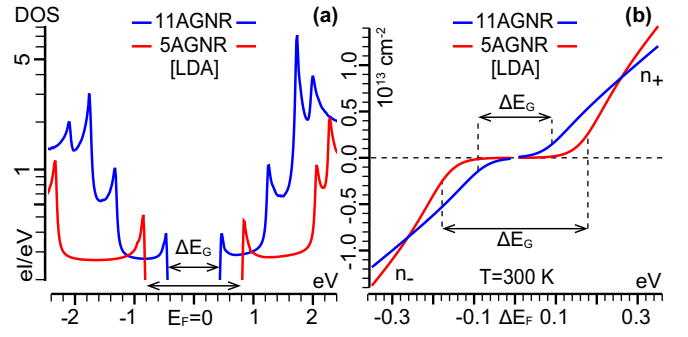

FIG. 3. (a) Density of states (DOS) and (b) charge carrier concentration at room temperature of 5AGNR and 11AGNR, computed from DFT-LDA. The DOS is plotted vs the band energies $\varepsilon_{\nu\mathbf{k}}$ relative to the intrinsic Fermi level ($E_F = 0$). The positive and negative charge carrier concentrations are reported vs the doping level ΔE_F. The minimum ΔE_F for charge carrier doping is $\Delta E_F = \pm\Delta E_G/2$.

An intraband and an interband plasmons were clearly spotted in all cases as distinct peaks in E_{LOSS}, on the bases of which we have fixed some general features of the two modes, which will be described in the following (Secs. IV A–IV C).

A. Intrinsic GNRs

The intrinsic (undoped) systems ($\Delta E_F = 0$) have a well-defined interband plasmon (InterP) and a tiny to negligible intraband plasmon (IntraP), activated by the minority fraction of excited electrons at room temperature, which produces an appreciable intensity only with the small band gap values provided by the LDA [Figs. 2(a) and 2(b)].

Such a *thermal* doping produces a square-root-like dispersion of the IntraP mode, which can be resolved only in the smallest band gap systems (5AGNR and 11AGNR with the LDA electronic structure). Indeed, the IntraP loss peak increases in intensity with increasing temperature, and may have a significant impact above ~500–700 K, depending on the band gap; see Appendix E.

On the other hand, the InterP loss peak presents a (linearly) increasing dispersion vs the incident momentum above the band gap, i.e., the activation energy for the interband plasmon, computed in Figs. 2(c) and 2(d) under both the LDA and LDA-SO (*GW*-corrected) approximations. A similar trend was predicted by a NN TB approach [33], where, however, due to the absence of a band gap, the predictions of the InterP peak positions are underestimated by roughly the band gap value. Therefore, the TB method appears to be sufficiently reliable for large, i.e., small band-gapped, GNRs (~10 nm wide, and above).

B. Extrinsic GNRs with LDA band gap

Turning to extrinsic doping, we first consider the LDA electronic structure [Figs. 1 and 3(a)] under a longitudinal wave vector transfer $q \lesssim 0.0025$ Å^{-1}. Small injected (+) or ejected (−) charge carrier concentrations $n_\pm$, being such that $|n_\pm| \sim 3 \times 10^{12}$ cm^{-2} in 5AGNR and $|n_\pm| \sim 2 \times 10^{12}$ cm^{-2} in 11AGNR, produce Fermi level shifts or doping levels just above or below the activation threshold for charge carrier

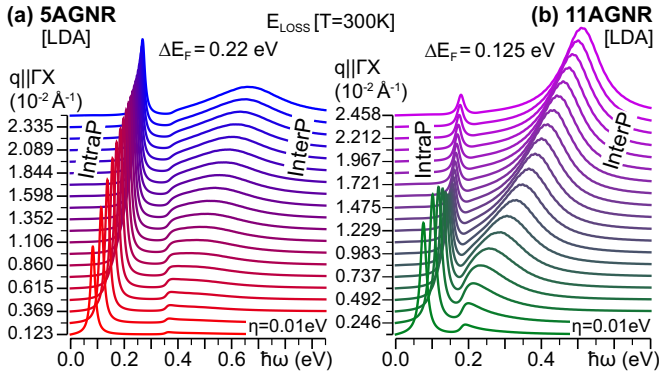FIG. 4. Room-temperature plasmon structure (E_{LOSS}) of doped 5AGNR (a) and 11AGNR (b), for $\hbar\omega \leqslant 1.0$ eV and $q \leqslant 0.0025$ Å^{-1}, parallel to the GNRs' axis. The doping concentrations [$n_+ \sim 6 \times 10^{12}$ cm^{-2} in (a), $n_+ \sim 3 \times 10^{12}$ cm^{-2} in (b)] induce moderate Fermi energy shifts, which leave the IntraP and InterP modes separated, with small overlap.

doping ($\pm\Delta E_{\text{G}}/2$ with $E_{\text{F}} = 0$) [Fig. 3(b)]. Under these conditions, the IntraP and InterP modes display similar intensities and appear to be uncorrelated with negligible overlap of the associated line shapes [see also Figs. 7(a) and 7(b)].

The overlap (interaction) region of the two plasmons becomes more and more effective with increasing $|n_\pm|$, in the range of $\sim 5 \times 10^{12}$–10^{13} cm^{-2} for 5AGNR and $\sim 3 \times 10^{12}$–5×10^{12} cm^{-2} for 11AGNR (Fig. 4).

Larger doping levels, corresponding to charge carrier concentrations $|n_\pm| \gtrsim 10^{13}$ cm^{-2} in 5AGNR and $|n_\pm| \gtrsim 5 \times 10^{12}$ cm^{-2} in 11AGNR, if achievable, lead to even stronger correlations, which results in the IntraP and InterP line shapes, being substantially superimposed. Such heavy conditions prevent the two modes from being distinguished in momentum space (Fig. 5), which allows them to be resolved in real space, e.g., by infrared imaging techniques [27].

The preliminary considerations made so far show that a fine-tuning of the doping conditions can isolate or mix the in-
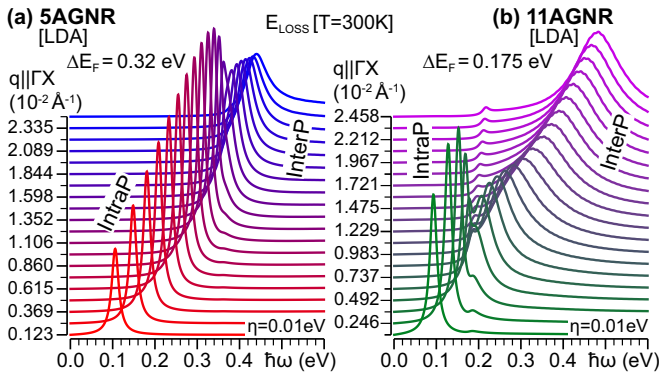

FIG. 5. Room-temperature plasmon spectrum (E_{LOSS}) of doped 5AGNR (a) and 11AGNR (b) for $\hbar\omega \leqslant 1.0$ eV and longitudinal $q \leqslant 0.0025$ Å^{-1}. The doping concentrations [$n_+ \sim 1.2 \times 10^{13}$ cm^{-2} in (a), $n_+ \sim 5 \times 10^{12}$ cm^{-2} in (b)] induce large Fermi energy shifts, which, in turn, cause the IntraP and InterP modes to be strongly correlated, and almost indistinguishable from each other.
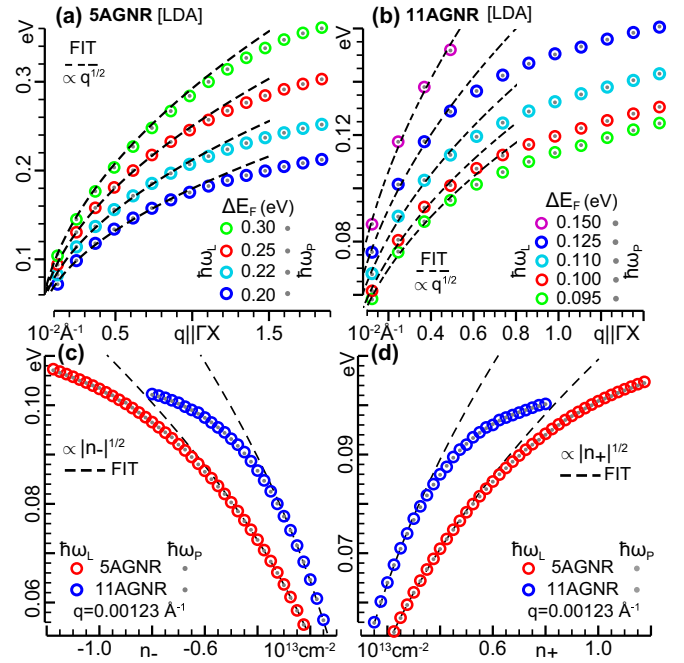

FIG. 6. IntraP loss-peak and resonance energies ($\hbar\omega_{\text{L}}$ and $\hbar\omega_{\text{P}}$) of 5AGNR and 11AGNR, reported in (a), (b) vs the applied wave vector $q\|\Gamma X$, and in (c), (d) vs charge carrier concentrations $n_\pm$ at room temperature. The black dashed lines label the scaling laws $\hbar\omega_{\text{P(L)}} \propto q^{1/2}$ [(a), (b)] and $\hbar\omega_{\text{P(L)}} \propto |n_\pm|^{1/2}$ [(c), (d)], obtained by fitting the numerical data at $q < 0.008$–0.010 Å^{-1} and $|n_\pm| < 0.5 \times 10^{13}$ cm^{-2}, respectively.

traband and interband plasmons, for the desired functionality of the GNR-based application [52].

As a marginal note, the behavior of the loss peaks with reversing the charge carrier sign reflects the slight asymmetric dispersions of the first VB and CB (Fig. 1). However, a non-negligible difference in the IntraP and InterP modes, at opposite ΔE_{F}, is appreciable in 5AGNR only (Appendix F), at a sufficiently large doping level ($|\Delta E_{\text{F}}| > 0.27$ eV) and longitudinal momentum transfer ($q > 0.01$ Å^{-1}). Like in graphene, a much more pronounced asymmetry may be obtained by exposure to chemical doping [53,54].

A more critical issue is the relation of the IntraP resonances $\hbar\omega_{\text{P}}$ [second zero of Re(ϵ^{M})], or the lowest E_{LOSS} peak energies $\hbar\omega_{\text{L}}$, to the longitudinal momentum $\hbar\mathbf{q}\|\Gamma X$. Indeed, as shown in Fig. 6, $\hbar\omega_{\text{P}}$ and $\hbar\omega_{\text{L}}$ are always so close that they can be confused with each other, notwithstanding $\hbar\omega_{\text{P}} < \hbar\omega_{\text{L}}$.

Furthermore, Figs. 6(a) and 6(b) respectively report the dependence of $\hbar\omega_{\text{P(L)}}$ vs q at fixed Fermi energy shifts $\Delta E_{\text{F}} = 0.20$–$0.30$ eV for 5AGNR and $\Delta E_{\text{F}} = 0.095$–$0.125$ eV for 11AGNR. Besides a general increasing trend, the q-$\hbar\omega_{\text{P(L)}}$ data sets are well correlated by a square-root law of the form $\hbar\omega_{\text{P(L)}} \propto q^{1/2}$, at applied wave vectors below 0.006 Å^{-1} in 11AGNR, and 0.010 Å^{-1} in 5AGNR, confirming the 2D nature of the intraband oscillation.

Similarly, a monotonically increasing behavior of $\hbar\omega_{\text{P(L)}}$ vs the positive or negative charge carrier concentration $n_\pm$ is detected, in both 5AGNR and 11AGNR, and displayed in Figs. 6(c) and 6(d), where the above-mentioned asymmetry of the first VB and CB is manifested in the slightly different val-
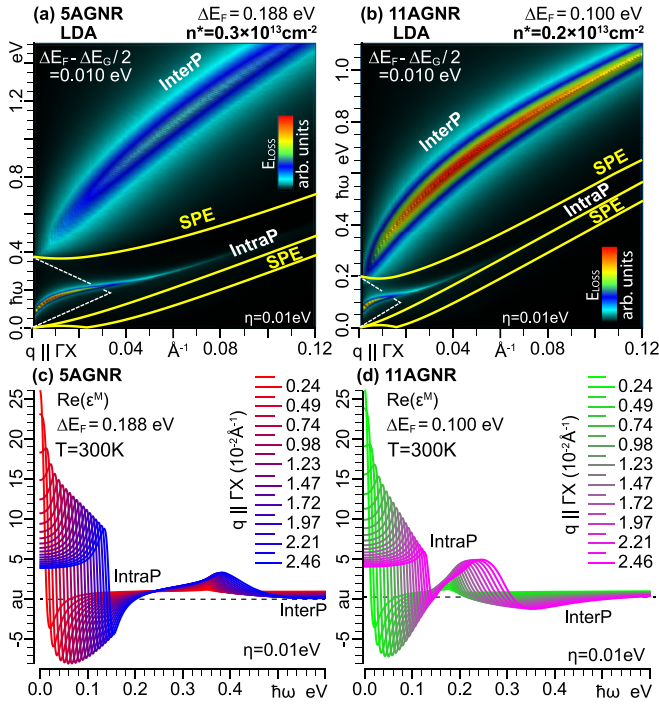
FIG. 7. Loss function E_{LOSS} [in arbitrary units, (a), (b)] and macroscopic real permittivity Re(ϵ^M) [in Hartree atomic units, (c), (d)] of 5AGNR [(a), (c)] and 11AGNR [(b), (d)], in the energy–wave vector domain $\hbar\omega \leqslant 1.0$ eV–$q \leqslant 0.12$Å^{-1}, with $q\|\Gamma X$. The intraband plasmon propagates outside the region of single-particle electron (SPE) transitions (yellow lines). The associated loss peaks $\hbar\omega_L$ correspond to well-spotted zeros of Re(ϵ^M) [(c), (d)]. The interband plasmon is, otherwise, dominant in the SPE region, where damping effects prevent Re(ϵ^M) from strictly achieving the plasmon resonance condition [(c), (d)]. The dashed white lines delimit the no-SPE region of graphene [55], for the corresponding value of the Fermi energy shift ΔE_F.

FIG. 8. Room-temperature loss spectra E_{LOSS} of 5AGNR (in atomic units), obtained with the ideal and optimized unit cells of Fig. 20, respectively, using the LDA (red) and GGA (blue). The two results are compared with the loss spectra derived from the LDA-SO (*GW*-corrected) approach (green). An identical doping concentration n_+ is simulated, which corresponds to Fermi energy shifts ΔE_F of 0.25, 0.285 eV (LDA), 0.349, 0.384 eV (GGA), and 0.907, 0.942 eV (*GW*).

ues $n_- > n_+$ at equal $|\Delta E_F|$. A square-root-like trend is also found in the different $n_\pm$-$\hbar\omega_{P(L)}$ data sets, for sufficiently low concentrations $|n_\pm| < 0.5 \times 10^{13}$ cm^{-2}, above the threshold for charge carrier doping.

A complete view of the propagation and interplay of the IntraP and InterP modes, within the LDA, is achieved by looking at the density plot profiles of E_{LOSS} on a wider energy-longitudinal wave vector domain, $\hbar\omega \leqslant 2.0$ eV–$q \leqslant 0.12$Å^{-1}, in conjunction with the zeros of the real permittivity Re(ϵ^M) [Eq. (4)].

The loss peaks associated with the IntraP mode occur in a region of the $(\hbar q, \hbar\omega)$ plane where single-particle excitation (SPE) processes (involving conduction electrons or valence holes) would be strictly forbidden at the absolute zero (no-SPE region). Thus, with the low thermal energies at hand, the intraband plasmon propagates practically undamped, in between the interband and intraband SPE regions [Figs. 7(a) and 7(b)], as attested by the clear (second) zeros in Re(ϵ^M) [Figs. 7(c) and 7(d)].

The no-SPE region of the GNRs includes that of graphene [55], and the IntraP peak (with its maximum intensity) lies within the no-SPE region of graphene, at small transferred momenta $q \lesssim \sqrt{\pi|n_\pm|}$ [55], which justifies the square-root-
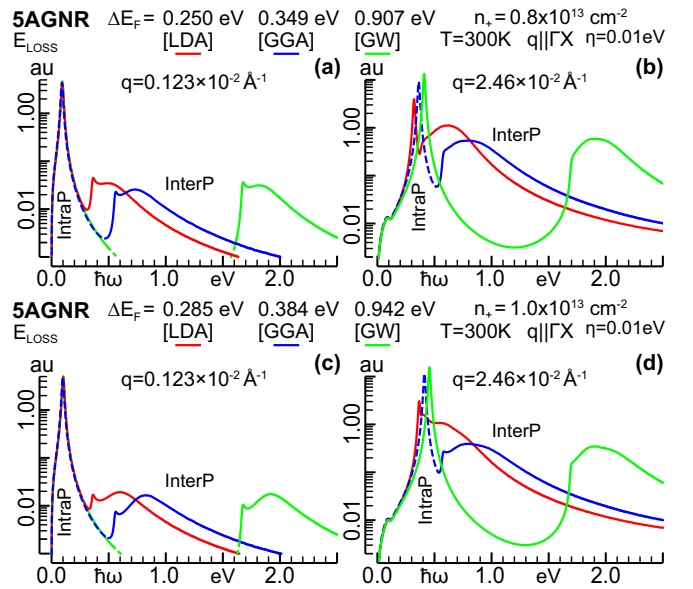
like dispersion reported in Fig. 6. Indeed, as suggested in Appendix G, by looking at the dielectric response of 29AGNR, the no-SPE region of armchair GNRs becomes more and more similar to the no-SPE region of graphene, as the GNR width increases.

The InterP loss peak, on the other hand, lies mostly inside the SPE region, which causes a significant damping of the mode, via interband electron-hole processes, attested by the missing zeros in the real permittivity above the band gap energy [see also Figs. 9(b) and 9(d)].

Also important to point out is that equal Fermi energy shifts on different GNRs [5AGNR, Figs. 7(a), 7(c), or 11AGNR, Figs. 7(b), 7(d)] are associated with different charge carrier concentrations [Fig. 3(b)] and produce distinct plasmon responses, which depend on GNR type and its peculiar electronic structure.

C. Band gap effect: LDA vs *GW*

We now come to the effect of band gap change, due to geometry relaxation (GGA optimization) or many-electron correlations (*GW* correction). To this purpose, we computed the LDA, GGA, and *GW*-corrected loss properties of 5AGNR and 11AGNR at identical (positive) doping concentrations, i.e., charge carrier injections associated with identical Fermi energy shifts relative to the activation threshold for charge carrier doping; see Figs. 8 and 9.

The first obvious consequence of increasing the band gap is that the InterP mode is accordingly shifted to higher energies, with its associated loss structure beginning at
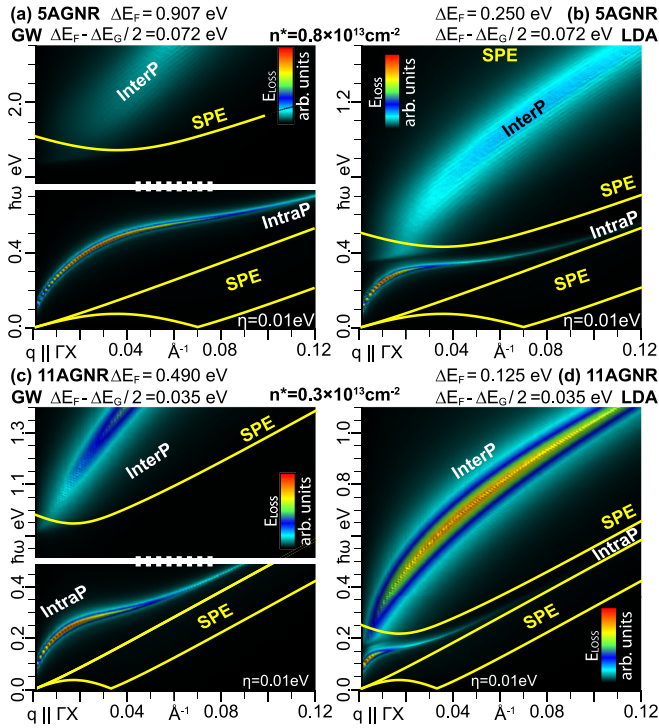
FIG. 9. Plasmon structure E_{LOSS} of 5AGNR [(a), (b)] and 11AGNR [(c), (d)], with the *GW*-corrected [(a), (c)] and LDA [(b), (d)] approaches, in the energy–longitudinal wave vector domain where the IntraP and InterP peaks display their maximum intensities ($\hbar\omega \leqslant 2.5$ eV–$q \leqslant 0.12$ Å^{-1}). Identical doping concentrations n_+ are simulated, which correspond to the Fermi energy shifts $\Delta E_{\text{F}} - \Delta E_{\text{G}}/2 = 0.072$ eV [(a), (b)] and 0.035 eV [(c), (d)], relative to the activation threshold for charge carrier doping (Fig. 3).

$\hbar\omega = \Delta E_{\text{G}}$. For example, in 5AGNR the InterP loss peak begins at ~0.36 eV, ~0.55 eV, and ~0.67 eV, with the LDA, GGA, and *GW*-corrected electronic structures, respectively, as reported in Fig. 8. The peak intensity is attenuated toward higher energies, because of the decreasing behavior of the dynamic factors in the unperturbed susceptibility of Eq. (2), provided by the retarded Green's functions ($\omega + \varepsilon_{\nu\mathbf{k}} - \varepsilon_{\nu'\mathbf{k}+\mathbf{q}} + i\eta)^{-1}$. This fact is independent of the doping conditions, as attested by intrinsic response of the systems [Figs. 2(c) and 2(d)].

Furthermore, in intrinsic GNRs the band gap increase further attenuates the thermally activated IntraP mode, which is practically absent in 5AGNR, with the *GW*-corrected electronic structure, for working temperatures below 1500 K; see Fig. 24 of Appendix F. Charge carrier injection or ejection, besides activating a strong intraband plasmon, opens an interaction (overlap) region between the IntraP and InterP modes, which is modulated by the charge carrier concentration (doping level) and transferred momentum. Then, under sufficiently weak interaction (negligible overlap) conditions, the IntraP loss peak is rather insensitive to band gap changes. This is the case in Figs. 8(a) and 8(c), where moderate to large Fermi energy shifts in 5AGNR are associated with small longitudinal wave vectors, of about ~0.01 Å^{-1}, with the IntraP peak preserving its line shape and position. A similar band gap independence can be observed in Fig. 9, with moderate charge
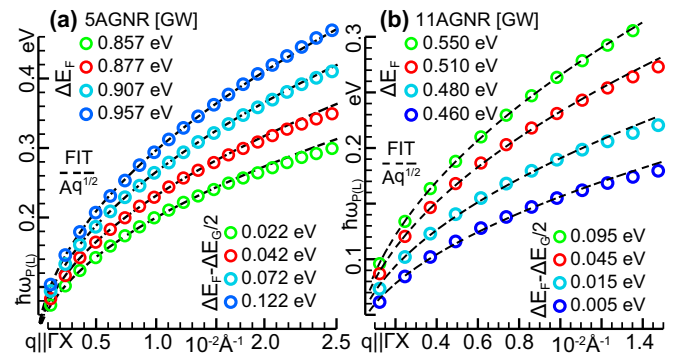

FIG. 10. IntraP resonance or loss-peak energies $\hbar\omega_{\text{P(L)}}$ of 5AGNR (a) and 11AGNR (b) vs the applied wave vector $q\|\Gamma X$, computed under the *GW*-corrected approach. The black dashed lines label the scaling laws $\hbar\omega_{\text{P(L)}} \propto q^{1/2}$ obtained by fitting the numerical data at $q < 0.015$–0.020 Å^{-1}.

carrier injections, equivalent to $\Delta E_{\text{F}} = 0.250$ eV in 5AGNR and $\Delta E_{\text{F}} = 0.125$ eV in 11AGNR, associated with small momentum transfers, i.e., longitudinal wave vectors below ~0.01 Å^{-1}; see also Fig. 3(b).

Conversely, non-negligible InterP-IntraP interactions in the LDA spectrum, due to an increase of the doping concentration and/or the transferred momentum, lead to correlated plasmon spectra, which significantly differ, in both the IntraP and InterP components, from the loss profiles obtained with the optimized GGA and *GW*-corrected approaches. In particular, sufficiently large longitudinal wave vectors, say, above ~0.15 Å^{-1}, at moderate to large doping injections, $\Delta E_{\text{F}} = 0.250$–0.285 eV, produce significantly different peak positions and intensities of the IntraP and InterP modes of 5AGNR, as shown in Figs. 8(b) and 8(d).

It is worth noticing, however, that the increase in resonance energy due to *GW* effects is somehow contrasted with the electron-hole interaction, operating to decrease the InterP peak position. A careful analysis of this effect would require a full *GW* plus Bethe-Salpeter equation (BSE) simulation [56], which however has practical limitations on the **k**-point sampling and the low-dimensional cutoff on the interaction kernel. More importantly, the main message of the present study is that even a small band gap variation (such as in the LDA vs GGA case) may result in a substantial change of the dielectric properties of the systems, as evidenced in Fig. 8(d).

In addition, the moderate doping concentrations, shown in Fig. 9, produce markedly distinct LDA and *GW* IntraP line shapes, at large longitudinal wave vectors $q > 0.02$ Å^{-1}. Indeed, the large *GW* band gaps come with a wide no-SPE region, which ensures the intraband plasmon a better control of the propagation environment. As a consequence, the IntraP mode has a more clear tendency to mimic the plasmon of a 2D free gas, with its resonance energies being better correlated, and for longer wave vector ranges, with the square-root law $\hbar\omega_{\text{P(L)}} \propto q^{1/2}$, than the LDA resonance energies, as can be deduced by looking at Figs. 6 and 10.

These considerations can be of help in cases where a significant band gap reduction results from the interaction of the GNR array with a contacting substrate [37], which is also one possibility for IntraP/InterP tuning.
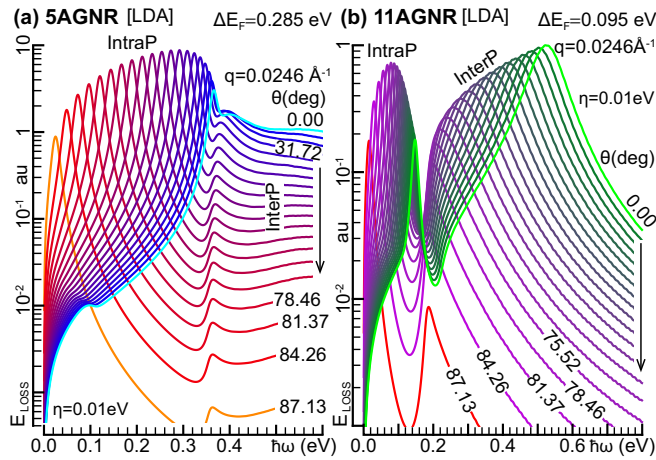
FIG. 11. Room-temperature loss curves of doped 5AGNR (a) and 11AGNR (b), with the LDA electronic structure, probed by different oblique wave vectors **q**, of fixed modulus $q = 0.0246$ Å^{-1} and inclination θ in the range of 0 to 87.13°, with respect to the GNRs' axis (ΓX), corresponding to $0.05 \leqslant \cos\theta \leqslant 1.00$ in steps of 0.05.

D. Oblique momentum

So far, we have discussed the plasmon activity of atomically precise GNR arrays with respect to longitudinal momentum transfers and a number of internal or external tunable parameters (GNR type, geometry, many-electron interaction, doping, and working temperature). Other major controlling factors, such as the GNR chirality and asymmetric edge passivation, would require different simulations.

In what follows, we report on how the interplay between IntraP and InterP modes is also strongly modulated by an in-plane incident momentum with inclination θ, relative to the GNR axis, thus characterizing the oblique plasmons of 5AGNR and 11AGNR at eV energies.

In this respect, we should recall that the unperturbed susceptibility of Eq. (2) is entirely determined by the KS structure of the PW-DFT step (Sec. II). The latter disperses only along the longitudinal crystal momentum ($\hbar\mathbf{k}\|\Gamma X$), because contiguous GNRs have been placed sufficiently far apart that their unperturbed charge densities are (numerically) nonoverlapping.

Accordingly, due to the difference in the statistical factors at the numerator of Eq. (2), each applied wave vector **q** of modulus $q = |\mathbf{q}|$ contributes with its ΓX component $q_x = q\cos\theta$ to the unperturbed susceptibility $\chi^0_{\mathbf{GG}'}$. On the other hand, the truncated interaction $v_{\mathbf{GG}'}$ of our TDDFT-RPA-2D approach [Eq. (A5)] is sensitive to the entire wave vector, and decreases with increasing its modulus.

In this *momentum mismatch* lies the atomistic mechanism by which the GNR arrays react to an external inclined momentum **q**. Figures 11, 12, and 13 show that, at any fixed q, both the IntraP and InterP modes are shifted to lower energies by increasing θ, from 0 to 90°, i.e., rotating the **q** orientation from longitudinal to transverse, with the InterP peak having a lower bound at the band gap energy.

Then, the interaction or overlap region of the intraband and interband plasmons, and the plasmon activities of the two modes, can be finely reduced or adjusted by operating on the
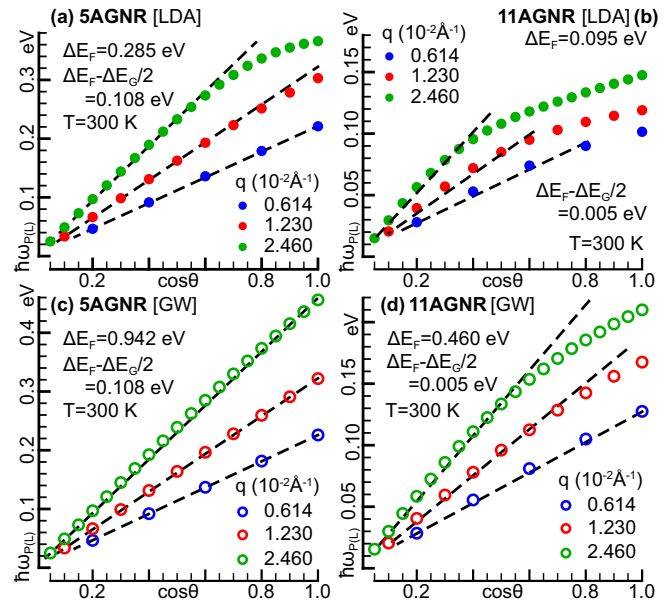

FIG. 12. Intraband plasmon dispersions of doped 5AGNR [(a), (c)] and 11AGNR [(b), (d)], with the LDA and *GW*-corrected electronic structures, probed by different oblique wave vectors **q**, of fixed modulus $q = 0.0246$ Å^{-1} and inclination θ in the range of 0 to 87.13°, with respect to the GNRs' axis (ΓX).

incident momentum direction. This is the case of Fig. 11, showing the LDA loss properties 5AGNR and 11AGNR at several inclined wave vectors, of fixed length $q \sim 0.025$ Å^{-1}, and sufficiently large doping injections, which induce a strong overlap of the two plasmons for a longitudinal momentum transfer. In particular, an oblique momentum with $\theta \gtrsim 30°$ in 5AGNR allows us to completely decouple the InterP and IntraP features. Also important to notice is that both the IntraP and InterP intensities decrease with θ coming near the perpendicular direction across the ΓX axis.

As for the plasmon resonance (or loss-peak) dispersions, both the IntraP and InterP loss peaks follow an increasing
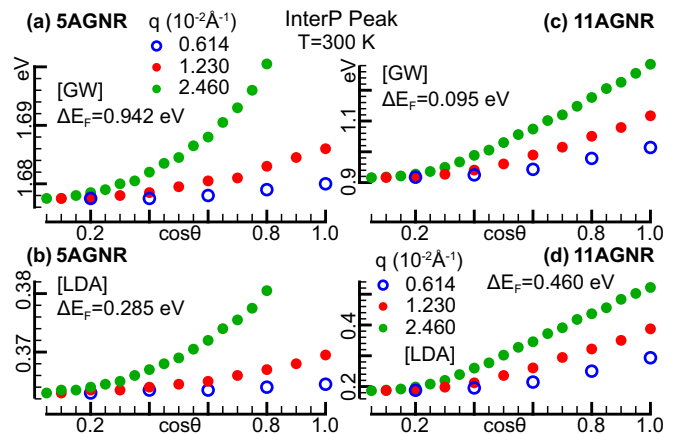

FIG. 13. Interband plasmon dispersions of doped 5AGNR [(a), (b)] and 11AGNR [(c), (d)] with the LDA and *GW*-corrected electronic structures, probed by different oblique wave vectors **q**, as in Fig. 12.

trend vs $\cos\theta = q_x/q$, at fixed q, respectively reported in Figs. 12 and 13. For sufficiently small doping concentrations and/or transferred momenta, the two modes are well separated, and the $\cos\theta$-$\hbar\omega_{P(L)}$ data appear to be consistent with the linear relation $\hbar\omega_{P(L)} \propto \cos\theta$, shown in Fig. 12. The agreement with such a trend turns from fair or good to excellent in the large-gapped GNR arrays, whose electronic structure is corrected by *GW* effects.

On the other hand, significant to large deviations from the linear behavior are observed in cases where the IntraP and InterP peaks have a non-negligible overlap, such as in the small-gapped GNR arrays, predicted by the LDA. We may also extrapolate the two-plasmon behavior under an applied momentum with nearly transverse direction to the GNRs' axis ($\theta \sim 90°$).

The dispersions of Fig. 12 allow us to conclude that the intraband plasmon resonance vanishes as $\cos\theta$, for distinct fixed values of q, whereas the dispersions of Fig. 13 indicate that the interband plasmon has a peak value right above the onset of the mode, namely the band gap energy. Nonetheless, the plasmon peak intensities become smaller and smaller for $\theta \to 90°$, with the macroscopic dielectric function tending to its static limit (see also Sec. VI and Appendix I). Finite transverse plasmon intensities may be recovered either by applying a strong external perturbation, such as a high-intensity electromagnetic wave, which is outside the linear-response TDDFT framework presented here, or by reducing the vacuum distance between contiguous GNRs, in such a way that the electronic structure of the array gets dispersive features along the transverse axis [22].

V. THz BAND

We now analyze the dielectric response of our ultranarrow GNRs in the far- to mid-infrared band, with the same TDDFT-RPA-2D approach (Sec. III and Appendix A 2) applied to the eV range (Sec. IV). In the present context, the $\chi^0_{\mathbf{GG'}}$ matrix of Eq. (2) was acquired on a highly resolved KS structure from the PW-DFT step, consisting of a 20 000 **k**-point sampling of the ΓX segment. Accordingly, a frequency resolution of $\sim$0.01 THz and a wave vector resolution of $\sim$7400 cm^{-1} were used to sample the unperturbed density-density response of the KS electrons at $\omega \lesssim 400$ THz, including the smallest $N_{LF} \sim 60$ **G**-vectors. In addition, a damping parameter η, equivalent to a frequency of 0.1 THz, was adopted to distinguish the loss profiles and plasmon resonances. Again, as in the eV calculations of the former section, the plasmon spectra were computed by plugging $\chi^0_{\mathbf{GG'}}$ into Eqs. (3) and (4).

The focus here is on the intraband plasmon, lying at resonance frequencies below $\sim$10 THz, in a $(\mathbf{q},\omega)$ region where its propagation is well separated and, thus, negligibly affected by the interband plasmon. Hence, the THz features of the IntraP mode are independent of the band gap (associated with a frequency range of $\sim$50–400 THz). In other terms, the macroscopic permittivity $\mathrm{Re}(\epsilon^M)$ and loss function E_{LOSS} have identical profiles at $\omega \lesssim 20$ THz with the same Fermi energy shift $\Delta E_F - \Delta E_G/2$, relative to the charge carrier doping threshold, and the different DFT approaches of the present paper (Appendix H). Furthermore, the resonance frequencies of the IntraP mode (ω_P) are clearly defined in the second zero
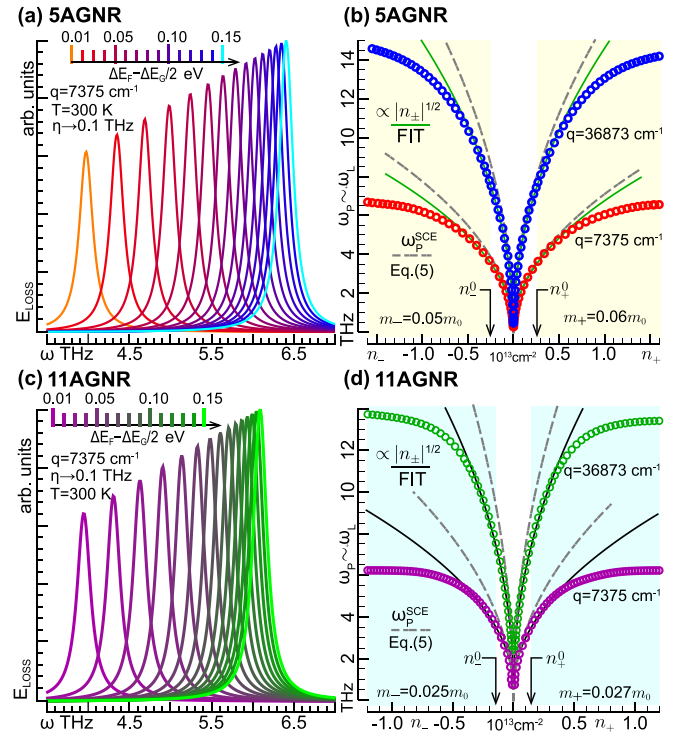

FIG. 14. Room-temperature loss curves E_{LOSS} [(a), (c)] and IntraP resonance frequencies ω_P or IntraP loss peak frequencies ω_L [(b), (d)] of extrinsic 5AGNR [(a), (b)] and 11AGNR [(c), (d)] over the THz band ($\omega < 10$ THz). Several doping conditions are considered, below and above the threshold concentration for charge carrier doping $n^0_\pm$ [black arrows in (b), (d)] at two different longitudinal wave vectors. The $\omega_{P(L)}$-$n_\pm$ data [(b), (d)] are fitted with the square-root law $\omega_{P(L)} \propto |n_\pm|^{1/2}$ for $|n_\pm| \lesssim 0.5$ cm^{-2} (continuous lines). The model of Eq. (5) is also tested (dashed lines), using $\theta = 0$ (longitudinal momentum) and the effective masses $m_\pm$ taken from the nonparabolic dispersions of Fig. 1 (with m_0 denoting the electron mass).

of the real permittivity (Appendix H) and indistinguishable from the IntraP peak frequencies (ω_L).

Based on the results of Figs. 6, 10, and 12, we may infer that the intraband plasmon frequency has a structure of the form $\omega_L \propto \cos\theta \sqrt{|n_\pm| q}$, for sufficiently low doping concentrations and small transferred momenta. Indeed, different non–*ab initio* approaches, including the SCE [32], suggest that the scaling law of the IntraP mode in the vacuum should be

$$\omega_P^{SCE} = \cos\theta \sqrt{q \frac{|n_\pm| e^2}{2\epsilon_0 m_\pm}}, \qquad (5)$$

with e denoting the electron charge. In the reminder of this section we will test Eq. (5) as a reliability factor for currently available non–*ab initio* tools at the THz level.

We first consider the behavior of the IntraP mode at two small sampled momenta, respectively associated with longitudinal wave vectors of 7375 and 36 873 cm^{-1}. The corresponding loss peak propagates undamped, with growing intensity, toward higher frequencies as the doping concentration increases [Figs. 14(a) and 14(c)]. This resonance is very well correlated with a square-root dependence on the charge
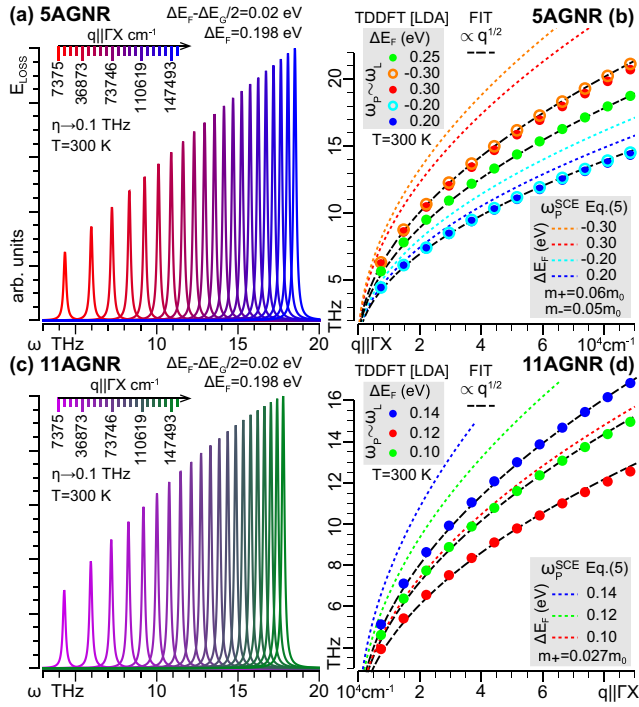
FIG. 15. Room-temperature loss curves [(a), (c)] and IntraP resonance frequencies [(b), (d)] of doped 5AGNR [(a), (b)] and 11AGNR [(c), (d)] over the THz band, with fixed doping levels and several longitudinal wave vectors. The $\omega_{P(L)}$-q dispersions [(b), (d)] are excellently correlated with a square-root law (dashed black lines), though the model of Eq. (5), with the same parameters as Fig. 14, gives an unreliable estimate of the intraband plasmon propagation (dashed blue lines).
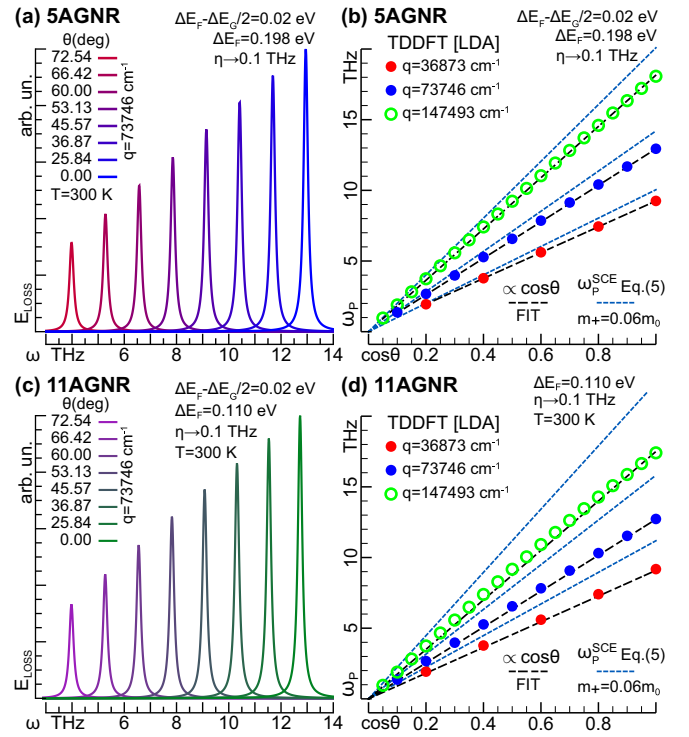
FIG. 16. Room-temperature loss curves [(a), (c)] and IntraP resonance frequencies [(b), (d)] of doped 5AGNR [(a), (b)] and 11AGNR [(c), (d)] over the THz band, with fixed doping levels and several oblique wave vectors (fixed modulus q, relative angle θ to the GNRs' axis). The $\omega_{P(L)}$-$\cos\theta$ data present an excellent linear correlation (dashed black lines), whose slope is, however, significantly overestimated by Eq. (5), with the same parameters as Figs. 14 and 15.

carrier concentration, for values typical of chemical doping or low gating [Figs. 14(b) and 14(d)], being such that the shifted Fermi level lies within the band gap range.

A $\omega_P \propto |n_\pm|^{1/2}$ law is also reasonably fulfilled for a small charge carrier doping concentration associated with a Fermi energy shift slightly above the first CB [Figs. 14(b) and 14(d)] or below the first VB, similarly to the eV band [Figs. 6(c) and 6(d)]. The range of validity of this trend becomes smaller and smaller with increasing q. The semiclassical model of Eq. (5), implemented using the effective masses derived from the Fermi velocity values of Fig. 1, provides only a qualitative agreement with the data, overestimating the asymmetry between positive and negative charge carriers. More importantly, values of $|n_\pm|$ larger than $\sim(0.4$–$0.5) \times 10^{13}$ cm^{-2} lead to a completely different trend, which may be catched only by a TDDFT-based modeling; see Sec. VI.

As a second issue, we characterize the IntraP oscillation as a function of the longitudinal momentum, under fixed extrinsic conditions. In the examples of Fig. 15, the loss peak lies in a region of the (q, ω) plane where the peak intensity increases with increasing q, from $\sim 10^4$ to $\sim 10^5$ cm^{-1}. Complementarily, the loss peak energy follows a perfect square-root trend $\omega_{P(L)} \propto q^{1/2}$, which resembles the behavior of the IntraP mode on the eV band at $q \lesssim 0.01$ Å^{-1} [Figs. 6(a), 6(b), and 10]. This oscillation is, then, a genuine 2D plasmon, like in a 2D electron gas, with the semiclassical predictions of Eq. (5)

largely overestimating (by up to 95%) the proportionality constant of the $\omega_{P(L)}$ vs $q^{1/2}$ relation. The main reason for such a discrepancy stems from the non-square-root correlations in the $|n_\pm|$-$\omega_{P(L)}$ data (Fig. 14).

Finally, we look at the behavior of the intraband plasmon with the change of relative angle θ between the transferred momentum $\mathbf{q}$ and the longitudinal ΓX axis (Fig. 16). As in the eV band, the IntraP loss peak increases in intensity and shifts toward higher energies with the plasmon moving from transverse ($\mathbf{q}\perp\Gamma X$, $\theta = 90°$) to longitudinal propagation ($\mathbf{q}\|\Gamma X$, $\theta = 0$).

In this frequency range, the influence of the InterP mode is negligible, which allows for a perfect linear correlation between the intraband resonance (or loss peak) frequencies $\hbar\omega_{P(L)}$ and $\cos\theta = q_x/q$, at fixed wave vector modulus $q = |\mathbf{q}|$, while, again, the proportionality constant of the SCE model significantly overestimates the actual slope of the $\hbar\omega_{P(L)}$ vs $\cos\theta$ relation.

In summary, a scaling behavior of the kind $\omega_{P(L)} \propto \cos\theta\, q^{1/2}$ can be safely assumed for the THz plasmon, while a fine-tunability of the associated mode with the doping concentration requires a detailed knowledge of the GNRs' electronic structure, along with the dependence of the density of occupied or empty levels on the working temperature (Fig. 3). Then, only an *ab initio* strategy, like the one presented here, can properly address the IntraP features for design purposes.

VI. TDDFT-GUIDED MODELING

We conclude by presenting an effective analytical model for the loss function of 5AGNR and 11AGNR at transferred wave vectors **q**, with longitudinal component $q \cos \theta$ below ~ 0.003 Å^{-1}.

In this range, the effect of crystal local fields, i.e., the influence of the $\mathbf{G} \neq \mathbf{0}$, $\mathbf{G}' \neq \mathbf{0}$ elements in Eqs. (2) and (3), is mostly negligible [21,22,24,49,51,57,58]. Then, we may approximate the macroscopic permittivity ϵ^{M} with the nonlocal-field expression $\epsilon_{\mathrm{NLF}}^{\mathrm{M}} = \epsilon_0 (1 - v_{\mathbf{00}} \chi_{\mathbf{00}})$, obtained by reducing Eq. (3) to a scalar equation, with the $N_{\mathrm{LF}} = 1$ crystal local fields, so that the loss function reads $E_{\mathrm{LOSS}} \approx -\operatorname{Im}(1/\epsilon_{\mathrm{NLF}}^{\mathrm{M}})$.

We may further restrict the electronic structure to the first VB ($\nu = -1$) and CB ($\nu = 1$). Using the above-mentioned independence of Eq. (2) on the **k** components perpendicular to the longitudinal direction (Sec. III), and transforming the **k** summation in the continuous limit, the unperturbed susceptibility becomes

$$\chi_{\mathbf{00}} \approx \sum_{\nu, \nu' = \pm 1} \int_{-k_{\Gamma X}}^{k_{\Gamma X}} \frac{dk}{\pi L_y L} \frac{(f_{\nu k} - f_{\nu' k + q \cos \theta}) M_{\nu \nu'}^{k \, q \cos \theta}}{\hbar \omega + \varepsilon_{\nu k} - \varepsilon_{\nu' k + q \cos \theta} + i \eta}. \quad (6)$$

Here, the integration is performed over the longitudinal direction $\mathbf{k} \parallel \Gamma X$, with $k_{\Gamma X} = \pi / L_x$ being the length of the ΓX segment (Fig. 1), and L_x the longitudinal lattice constant of the GNR array, e.g., $L_x = 3 \times 1.42$ Å with the ideal GNR geometry detailed in Sec. I and Appendix B. The band energies, given in Eq. (1), enter the determination of the occupation factors, along with the shifted Fermi energy, namely the doping level. $L_y = (w + L)$ denotes the transverse lattice constant of the GNR array; see Fig. 20 of Appendix B.

To complete the picture, an analytical form is needed for the correlation terms

$$M_{\nu \nu'}^{k \, q_x} = |\langle \nu k | e^{-i q_x x} | \nu' k + q_x \rangle|^2. \quad (7a)$$

To this end, we used the different LDA eigensystems $\{\varepsilon_{\nu \mathbf{k}}, |\nu \mathbf{k}\rangle\}$, acquired from the KS structure in the PW-DFT step (Sec. II), to compute the matrix elements of the velocity operator $v_{\nu \nu'}(k) = \langle \nu k | -i \hbar \nabla / m | \nu' k \rangle$, whose diagonal components $v_{\nu \nu}(k)$ coincide with the group velocities $\partial \varepsilon_{\nu k} / \hbar \partial k$ [see also Appendix A 2, Eq. (A2)].

In Fig. 17(a), we show that these quantities are sufficiently well represented by the nonparabolic bands of Eq. (1), yielding

$$v_{\pm 1 \pm 1}(k) = \frac{\pm \hbar^2 v_{\pm}^2 k}{\sqrt{(\Delta E_{\mathrm{G}}/2)^2 + \hbar^2 v_{\pm}^2 k^2}}. \quad (7b)$$

As for the off-diagonal velocities, a tentative interpolation function of the form

$$|v_{1-1}(k)| = |v_{-11}(k)| = \frac{v_{\max} - v_{\min}}{\left(k^2 / k_0^2 + 1\right)^{3/2}} + v_{\min} \quad (7c)$$

was defined, which depends on two velocity parameters $v_{\max}$, $v_{\min}$ and a characteristic wave vector k_0, specific of the GNR type.
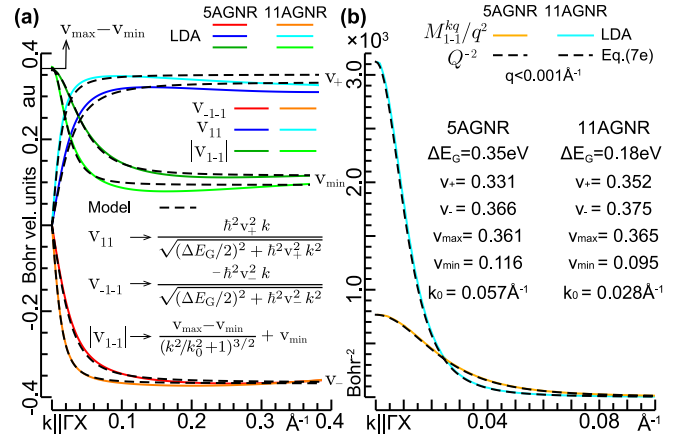

FIG. 17. (a) Matrix elements $v_{\nu \nu'}(k)$ of the velocity operator, $\nu, \nu' = \pm 1$ and (b) low-q expansion of the $M_{\nu \nu'}^{k \, q}$ matrix, $\nu, \nu' = \pm 1$, in comparison with the model of Eq. (7e), for 5AGNR and 11AGNR, at small longitudinal wave vectors $q < 0.001$ Å^{-1}.

With the velocity matrix at hand, we verified that the $\{M_{\nu \nu'}^{k \, q_x}\}_{\nu, \nu' = \pm 1}$ matrix, computed from Eq. (A1) at the LDA level, is excellently approximated by

$$M_{\pm 1 \pm 1}^{k \, q_x} \approx 1 - \frac{q_x^2}{Q(k)^2}, \quad (7d)$$

$$M_{\pm 1 \mp 1}^{k \, q_x} \approx \frac{q_x^2}{Q(k)^2}, \quad Q(k) = \frac{|\varepsilon_{1k} - \varepsilon_{-1k}|}{\hbar |v_{1-1}(k)|}. \quad (7e)$$

Here, the q_x^2 correction to the diagonal elements [Eq. (7d)] is negligible in the considered wave vector range, so that the crude expression $M_{\pm 1 \pm 1}^{k \, q_x} \approx 1$ is sufficiently reliable, within the normalization error of the numerical band states ($< 0.01\%$). This makes the structure of Eq. (6) similar to the unperturbed susceptibility of graphene, as calculated under the Dirac-cone approximation [55], with the obvious differences that the GNR arrays are gapped, 1D systems, with nonconstant group velocities. Furthermore, as reported in Fig. 17(b), the off-diagonal coefficients $M_{\pm 1 \mp 1}^{k \, q_x} / q_x^2$, obtained from Eq. (7e), have the dimension of square lengths, and are perfectly matched with the result of $k \cdot p$ *perturbation theory*, here denoted $Q(k)^{-2}$.

To keep the modeling as simple as possible, we approximate the RPA kernel $v_{\mathbf{00}}$ in $\epsilon_{\mathrm{NLF}}^{\mathrm{M}}$ with its vanishing-momentum-limit expression $v_{\mathbf{00}} \approx \frac{L}{2 \epsilon_0 q}$ [see Appendix A 2, Eq. (A5)], i.e., with the 2D Coulomb potential. Then, the macroscopic permittivity may be written as

$$\epsilon_{\mathrm{NLF}}^{\mathrm{M}} \approx \epsilon_0 - \sum_{\nu, \nu' = \pm 1} \int_{-k_{\Gamma X}}^{k_{\Gamma X}} \frac{dk}{2 \pi L_y q} (f_{\nu k} - f_{\nu' k + q \cos \theta})$$

$$\times \frac{\delta_{\nu \nu'} - \frac{\nu \nu' q^2 \cos^2 \theta}{Q(k)^2}}{\hbar \omega + \varepsilon_{\nu k} - \varepsilon_{\nu' k + q \cos \theta} + i \eta}. \quad (8)$$

It can be straightforwardly checked that $\epsilon_{\mathrm{NLF}}^{\mathrm{M}}$ correctly approaches the static limit $\epsilon_{\mathrm{NLF}}^{\mathrm{M}} \to 0$ as $q \cos^2 \theta$, for small or transverse wave vectors [see Appendix H, Eq. (I1)].

Indeed, Eq. (8) makes an excellent approximation to the *ab initio* permittivity (Sec. IV and Sec. V) for probing energies
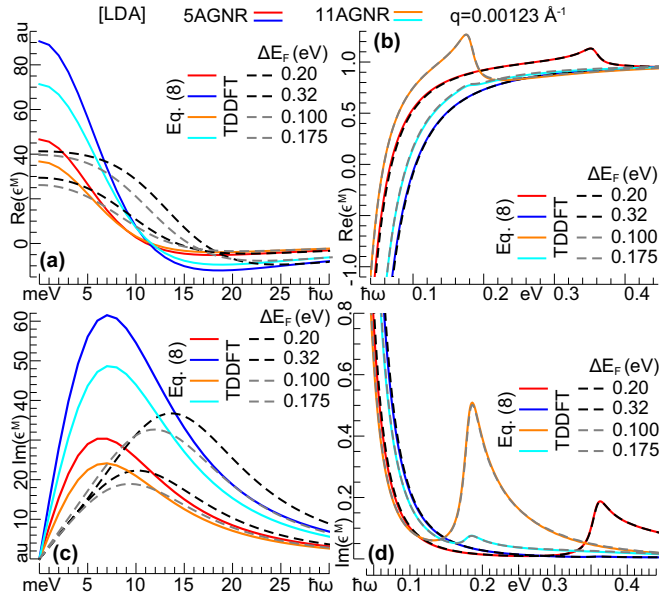
FIG. 18. Real [(a), (b)] and imaginary [(c), (d)] permittivity of 5AGNR and 11AGNR on the eV range, at room temperature and different doping levels, as calculated from the TDDFT-RPA-2D approach of Sec. IV and the analytical model of Eq. (8), at a small longitudinal wave vector. Notwithstanding the large discrepancies for $\hbar\omega < 0.02$ eV, the analytical and numerical results are perfectly matched for $\hbar\omega > 0.05$ eV.

much larger than $\sim\hbar|v_\pm|q$ and longitudinal wave vectors much smaller than $k_{\Gamma X}$ (Fig. 18).

For example, Eqs. (2)–(4) and Eq. (8) are in large disagreement with each other, in defining the structure of ϵ^M on the eV scale at $\hbar\omega \lesssim 0.01$ eV, with a doping level $\Delta E_F \gtrsim 0.1$ eV and a longitudinal wave vector of $\sim 10^{-2}$ Å^{-1}. The latter is associated with a characteristic energy $\hbar|v_\pm|q \sim 0.005$ eV [Figs. 18(a), 18(c)]. This significant mismatch is due to the exclusion of the $\mathbf{G}, \mathbf{G}' \neq \mathbf{0}$ components from Eq. (3), i.e., the neglect of crystal local fields [49,57], which must be taken into account in a correct estimation of first zero of $\mathrm{Re}(\epsilon^M)$, plus the line shape of the IntraP absorption peak in $\mathrm{Im}(\epsilon^M)$.

On the other hand, with the same parameters, the *ab initio* form of ϵ^M is perfectly matched with the non–*ab initio* approximation, leading to $\epsilon^M_{\mathrm{NLF}}$, at $\hbar\omega \gtrsim 0.05$ eV [Figs. 18(b), 18(d)]. In particular, the second zero of $\mathrm{Re}(\epsilon^M)$, i.e., the IntraP resonance, and the highest absorption peak in $\mathrm{Im}(\epsilon^M)$, related to the InterP mode, are accurately estimated by Eq. (8). A similar disagreement or agreement is detected on the THz scale, with a longitudinal wave vector of $\sim 10^4$ cm^{-1}, below or above a frequency of ~ 0.5 THz.

More importantly, the loss function of the systems, being vanishing at energies below the second zero of ϵ^M, is excellently reproduced by both Eqs. (2)–(4) and Eq. (8) in defining the intraband plasmon features at $q \lesssim 0.05$ Å^{-2} (Fig. 19). The agreement is also remarkably good on the interband plasmon behavior at $q \lesssim 0.02$ Å^{-2}. In contrast, at larger q values, Eq. (8) becomes inaccurate, because of both the neglect of crystal local fields and the exclusion of band states outside the first VB and CB [Fig. 19(a)]. At a closer look, a slight peak displacement is observed on the THz band, due to numerical
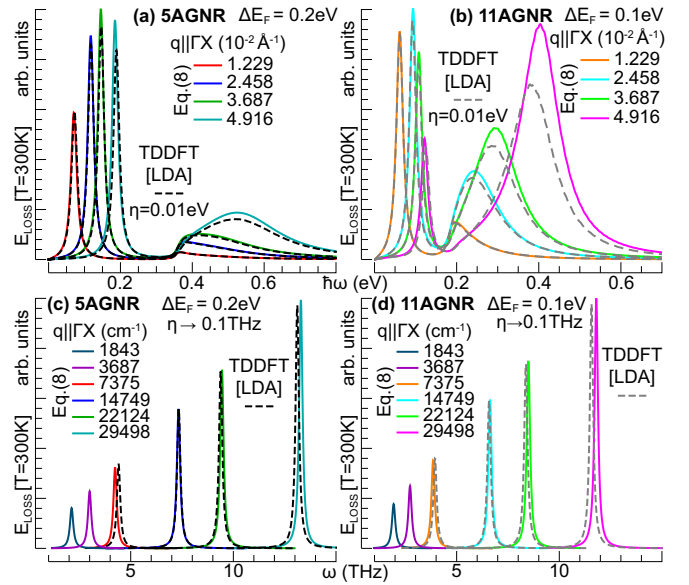

FIG. 19. Room-temperature plasmon spectra of 5AGNR and 11AGNR on the eV [(a), (b)] and THz [(c), (d)] ranges, at some fixed doping levels. Apart from a slight displacement, due to the normalization error on the numerical wave functions, the results from TDDFT (Sec. IV and Sec. V) and Eq. (8) are in excellent agreement, correctly reproducing both the IntraP and InterP features, at longitudinal wave vectors below ~ 0.003 Å^{-1}. An extrapolation of the loss function for very small wave vectors, below the resolution of TDDFT calculations, is also shown in [(c), (d)].

errors concerning the normalization of the DFT band states. Nonetheless, Eq. (8) allows us to extrapolate the intraband plasmon spectrum below the wave vector resolution of the TDDFT calculations [Fig. 19(b)].

The arguments presented in this section are suggestive that only a modeling assisted by *ab initio* tools can accurately define the plasmon properties of narrow GNRs, in a limited range of the tunable parameters.

VII. CONCLUSIONS

We have presented an *ab initio* analysis of plasmon excitation and dispersion in undoped and doped (or gated) armchair GNRs, of ultranarrow width, organized as ideal periodic 2D arrays, on the energy regime going from the eV to the THz scale.

We have used 5AGNR and 11AGNR as testing systems, and a TDDFT+RPA approach suitably designed for 2D materials, to unravel the effect of the electronic properties (band structure) on the plasmon response, along a broad range of longitudinal and oblique momenta to the GNR axis.

In this way, we have fully characterized two distinct collective oscillations, namely, an intraband plasmon and an interband plasmon, which are analogous to the *bulk* and *edge* plasmons, reported in a number of theoretical and experimental studies from nanoscale materials [15,16,21,25–29,32–36].

We have shown that the peak position of the InterP mode, assisted by one-electron processes between the first VB (of π character) and the first CB (of dominant π^* character), is weakly unaffected by doping, while it is mainly modulated by the GNR width.

On the other hand, the IntraP mode propagates undamped, being strongly influenced by (positive or negative) charge carrier doping, due to electron injection/ejection, or gating. The dispersion of this mode has a clear trend vs the incident momentum and its inclination, which shows some match with less sophisticated non–*ab initio* methods. Nonetheless, a full understanding of the exceptional plasmonics of the GNRs cannot be achieved without a proper simulation at the atomistic level.

An example of how to derive a reliable and ready-to-use modeling from TDDFT calculations has been presented, which may be extended to more complex nanoribbon systems.

Our calculations confirm that graphene nanoribbons (in planar array form) can be used as excellent platforms for the engineering of nanophotonic and nanoplasmonic devices; therefore, these findings call for more experimental investigations of their plasmonic properties and performances.

APPENDIX A: COMPUTATIONAL DETAILS

In this first Appendix, we discuss the computational details of the TDDFT-RPA-2D approach, outlined in Sec. II and Sec. III. All the computations were performed on the tier-0, high-performance computing (HPC) facility named *Marconi*, and owned by the CINECA Consortium (Italy).

1. DFT band structure

The ABINIT package (v8.4.2 [59]) was applied to three-dimensional (3D) slabs, respectively made of equally spaced distributions of 5AGNR and 11AGNR, at a distance L of 20 Å. Both the LDA [41] and GGA [42] approaches were implemented, in conjunction with standard norm-conserving pseudopotentials [43,44] to replace the core electrons.

The PW basis set $PW_{k+G}(r) = \Omega_0^{-1/2} e^{i(k+G) \cdot r}$ was used to define the KS valence electron states, as

$$|\nu k\rangle = N^{-1/2} \sum_G c_{\nu k+G} |PW_{k+G}\rangle. \qquad (A1)$$

In this expansion, Ω_0 is the unit cell volume, k a crystal wave vector in the first BZ, G a reciprocal lattice vector, ν the band index, and N the number of k points in the Monkhorst-Pack (MP) grid [60] sampling the first BZ. The number of the PWs in $|\nu k\rangle$ was restricted by the cutoff condition $|k + G|^2 \leqslant 180 \text{ Å}^{-2}$.

The chosen value of L ensured negligible overlap of the ground-state electron densities localized on contiguous GNRs. Consequently, the eigenvector coefficients $\{c_{\nu k+G}\}$, representing the $|\nu k\rangle$'s, turned out to be independent of the k-vector components perpendicular to the GNR axis, along with the associated eigenvalues $\varepsilon_{\nu k}$. In other words, the energy band dispersions were nonflat only along the GNR axis.

For this reason, both self-consistent and non-self-consistent methods could be safely applied on a uniform sampling of the irreducible 1D part of the first BZ, i.e., the ΓX segment parallel to the GNR axis [Fig. 20(b) of Appendix B]. Then, geometry optimization and ground-state calculations were, respectively, performed on $48 \times 1 \times 1$ and $60 \times 1 \times 1$ MP grids, including the lowest 24 (empty) conduction bands, above the 22 and 46 (occupied) valence bands, which respectively characterize 5AGNR and 11AGNR.

These calculations were cross-checked by the VASP package (v5.4.4 [61]), which also provided the atomic projected-band analysis for the systems (see Appendix D).

Subsequently, the KS structure $\{c_{\nu k+G}, \varepsilon_{\nu k}\}$ was refined on the ΓX segment in non-self-consistent runs carried out with ABINIT. The following, highly resolved MP meshes were used: (i) $1200 \times 1 \times 1$ k points, with the lowest 70 bands, for 5AGNR, and 100 bands, for 11AGNR, to sample the eV band, and (ii) $20\,000 \times 1 \times 1$ k points, with the lowest 40 bands, for 5AGNR, and 65 bands, for 11AGNR, to sample the THz band.

In both cases (i) and (ii), the ideal and optimized geometries of the GNRs were respectively processed by DFT-LDA and DFT-GGA. The LDA energy spectrum was further treated under the SO approximation [45] to account for *GW* band gap corrections [31]. A number of $\sim 10^5$ coefficients $\{c_{\nu k+G}\}$ per electron state $\varepsilon_{\nu k}$ were considered, equivalent to a normalization error below 0.01%. The velocity matrix, defined in Sec. VI and reported in Fig. 17(a), for states in the first VB and CB, was calculated as

$$v_{\nu\nu'}(k) = \frac{\hbar k}{m} \delta_{\nu\nu'} + \sum_G c_{\nu k+G}^* \frac{\hbar G}{m} c_{\nu' k+G}, \qquad (A2)$$

with m denoting the electron mass.

2. Dielectric response of the KS electrons

The KS structure acquired from the output files, related to DFT-LDA, DFT-GGA, and DFT-LDA-SO calculations, was processed by a FORTRAN MPI-parallel code, originally written by M.P. and subsequently developed by A.S. [21,22,24,46,51,58,62,63]. With this TDDFT code, the unperturbed density-density matrix $\chi_{GG'}^0$ of Eq. (2) was acquired mostly at room temperature, with the exception of the plots in Appendix E, under a broad range of intrinsic and extrinsic conditions, input energies, and longitudinal and oblique momenta over the eV (i) and THz (ii) bands.

The correlation coefficients in Eq. (2) were computed as

$$\rho_{\nu\nu'}^{kq}(G) = \sum_{G'} c_{\nu k+G'}^* \, c_{\nu' k+q+G+G'}. \qquad (A3)$$

Near-infrared to visible (i) and mid- to far-infrared (ii) calculations were respectively performed by including the contributions to Eq. (2) from the energy ranges $\hbar\omega \leqslant 4.0$ eV and $\hbar\omega \leqslant 2.5$ eV, with an energy resolution of 0.5 meV and 0.01 THz, plus a damping parameter η of 0.01 eV and 0.1 THz. The leading term in Eq. (A3), used to derive the approximated analytical forms of Eqs. (7d) and (7e), was computed as

$$\rho_{\nu\nu'}^{kq}(0) = \sum_G c_{\nu k+G}^* \, c_{\nu' k+q+G}. \qquad (A4)$$

The central equation of TDDFT (3) was solved with the smallest $\sim$100 (i) and $\sim$60 (ii) reciprocal lattice vectors $\mathbf{G}$, $\mathbf{G}'$, of parallel component $\mathbf{g}$, $\mathbf{g}'$ and perpendicular components G_z, G_z', to the plane of the GNR arrays. In all cases an in-plane wave vector $\mathbf{q}$ was applied, of inclination $\theta \geqslant 0$ relative to the longitudinal direction, parallel to the GNRs' axis.

A local kernel was included in Eq. (3), based on the modified local interaction

$$v_{\mathbf{GG}'} = \frac{\delta_{\mathbf{gg}'} d_{G_z G_z'}^{|\mathbf{q}+\mathbf{g}|}}{2\epsilon_0 |\mathbf{q}+\mathbf{g}|},$$

$$d_{G_z G_z'}^{|\mathbf{q}+\mathbf{g}|} = \int_{-L/2}^{L/2} dz \int_{-L/2}^{L/2} dz' e^{i(G_z z - G_z' z') - |\mathbf{q}+\mathbf{g}||z+z'|}, \quad \text{(A5)}$$

having the form of a 2D truncated Coulomb potential, at the half-distance between nearest-neighbor GNR-array planes [21,46,50,51], with diagonal matrix elements

$$v_{\mathbf{GG}} = \frac{1}{2\epsilon_0 |\mathbf{q}+\mathbf{G}|^2}\left(1 + \frac{1 - e^{-L|\mathbf{q}+\mathbf{g}|}}{L|\mathbf{q}+\mathbf{g}|}\frac{G_z^2 - |\mathbf{q}+\mathbf{g}|^2}{|\mathbf{q}+\mathbf{G}|^2}\right)$$
$$\text{(A6)}$$

and leading component

$$v_{\mathbf{00}} = \frac{1}{2\epsilon_0 q^2}\left(1 - \frac{1 - e^{-Lq}}{Lq}\right), \quad \text{(A7)}$$

tending to the 2D Coulomb potential form $v_{\mathbf{00}} \to \frac{L}{2\epsilon_0 q}$, in the vanishing-momentum limit.

In this TDDFT-RPA-2D framework, the macroscopic dielectric and loss functions of the 5AGNR and 11AGNR arrays were respectively determined by Eq. (4).

APPENDIX B: GEOMETRY OPTIMIZATION

We now provide the details of the geometry optimizations performed with the PW-DFT tools, introduced in Sec. II and detailed in Appendix A 1, under the LDA and GGA. In DFT approaches, the positions of all H and C atoms of the GNR arrays were relaxed, with fixed unit cell shape and volume, on an MP grid of $48 \times 1 \times 1$ points, along the irreducible part of the ΓX segment.

The optimized bond distances (d_i) and angles (α_i), in the unit cells of 5AGNR and 11AGNR, were thus calculated, as respectively reported in Figs. 20(a) and 21(a). The same panels provide the average C-C and C-H bond lengths and bond angles, in comparison with the ideal or nominal (NOM) values quoted in Sec. II.

Figure 20(b) displays a sketch of a periodic space distributions of GNRs, highlighting the ΓX direction and the 20 Å vacuum between contiguous elements. Figures 20(c) and 21(b) show the positions of the unit cell atoms in the optimized and nonoptimized geometries.

As pointed out in Sec. II, the optimized and ideal positions of the unit cell atoms differ by less than $\sim$4% (with the LDA) and $\sim$3.8% (with the GGA). Indeed, the LDA values are slightly smaller than the GGA values, which confirms the overbinding character of the LDA. The largest differences occur at the edges of the GNRs, with the most external C-C
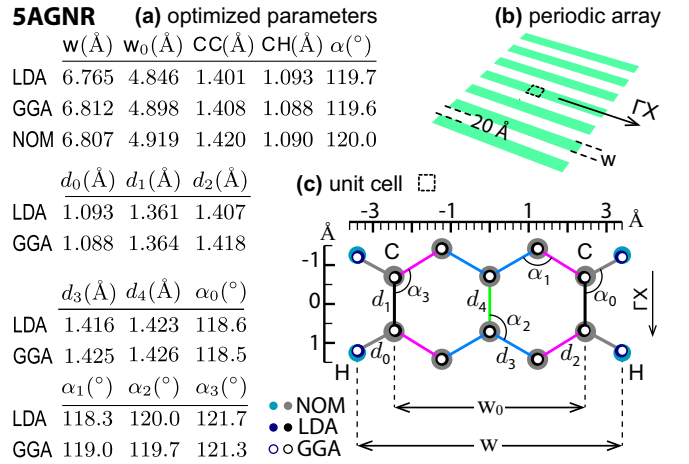

5AGNR   **(a) optimized parameters**   **(b) periodic array**

	w(Å)	w_0(Å)	CC(Å)	CH(Å)	α(°)
LDA	6.765	4.846	1.401	1.093	119.7
GGA	6.812	4.898	1.408	1.088	119.6
NOM	6.807	4.919	1.420	1.090	120.0

	d_0(Å)	d_1(Å)	d_2(Å)
LDA	1.093	1.361	1.407
GGA	1.088	1.364	1.418

	d_3(Å)	d_4(Å)	α_0(°)
LDA	1.416	1.423	118.6
GGA	1.425	1.426	118.5

	α_1(°)	α_2(°)	α_3(°)
LDA	118.3	120.0	121.7
GGA	119.0	119.7	121.3

(c) unit cell

FIG. 20. Structural information on the 5AGNR array. (a) C-H bond length d_0, C-C bond length d_i, $i = 1, \ldots, 4$, and bond angles α_i, $i = 0, \ldots, 4$, obtained within the LDA and GGA; the averages of these three quantities, respectively denoted CH, CC, and α, are reported along with the GNR widths w and w_0 (respectively obtained by including and excluding the passivating H atoms); the nonoptimized values (labeled NOM) are also given for reference purposes. (b) Sketch of a periodic planar array of the 5AGNR type. (c) Optimized and ideal positions of the unit cell atoms in Å.

bonds reduced to 1.36–1.37 Å and the H-C-C bond angles narrowed to 118.5°–118.6°.

We may further notice a reduction in the *benzenoid* edge structures, i.e., the areas of the most external hexagons of C atoms, of 2.0%–2.5% (with the LDA) and 1.0%–1.5% (with
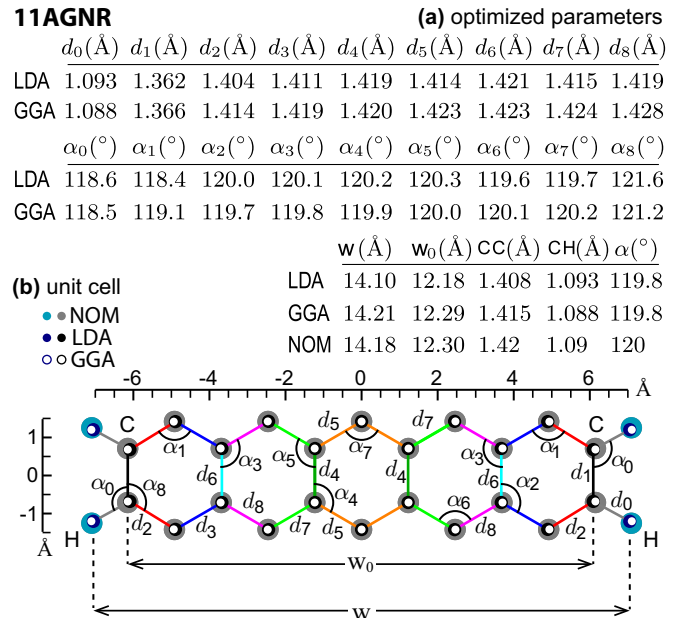

11AGNR   **(a) optimized parameters**

	d_0(Å)	d_1(Å)	d_2(Å)	d_3(Å)	d_4(Å)	d_5(Å)	d_6(Å)	d_7(Å)	d_8(Å)
LDA	1.093	1.362	1.404	1.411	1.419	1.414	1.421	1.415	1.419
GGA	1.088	1.366	1.414	1.419	1.420	1.423	1.423	1.424	1.428

	α_0(°)	α_1(°)	α_2(°)	α_3(°)	α_4(°)	α_5(°)	α_6(°)	α_7(°)	α_8(°)
LDA	118.6	118.4	120.0	120.1	120.2	120.3	119.6	119.7	121.6
GGA	118.5	119.1	119.7	119.8	119.9	120.0	120.1	120.2	121.2

	w(Å)	w_0(Å)	CC(Å)	CH(Å)	α(°)
LDA	14.10	12.18	1.408	1.093	119.8
GGA	14.21	12.29	1.415	1.088	119.8
NOM	14.18	12.30	1.42	1.09	120

(b) unit cell

FIG. 21. Structural information on the 11AGNR array with the same notation as Fig. 21. (a) C-H, C-C bond lengths d_i, bond angles α_i, $i = 0, \ldots, 8$, and widths w, w_0 obtained within the LDA and GGA, and compared with ideal values from the nonoptimized unit cell (NOM). (b) Positions of all C and H in the unit cell.
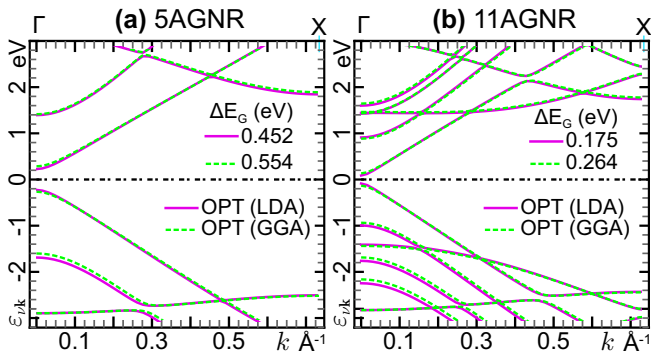
FIG. 22. Energy bands of 5AGNR (a) and 11AGNR (b), calculated from the optimized unit cells of the corresponding arrays, within the LDA (magenta) and GGA (dashed green).

FIG. 23. Energy bands of 5AGNR (a) and 11AGNR (b), atomically projected onto the s-p_x-p_y (σ, σ^*) and p_z (π, π^*) orbitals, with the GNR array lying on the xy plane, as sketched in Fig. 20(b). The contribution of d orbitals, included in this calculation, is negligibly small.

the GGA). All other bond lengths and angles in the systems are practically indistinguishable from the ideal values, within an error below ∼0.4%.

These results show that the main effect of geometry optimization is in the ends of the GNR structures, i.e., in the way the C atoms have been passivated. Other forms of passivation, with inclusion of edge-roughness deformations due to asymmetric defects [28], produce more significant changes in the unit cell geometries.

APPENDIX C: OPTIMIZED ELECTRONIC STRUCTURE

A visual inspection of the LDA and GGA energy bands of the optimized systems, reported in Fig. 22, suggests that the atomic position relaxations of Figs. 20(c) and 21(b) play a marginal role in the dispersion profiles within ±3 eV from the Fermi energy. In this energy window, the average difference between the LDA and GGA bands is less than 0.04 eV for 5AGNR and 0.06 eV for 11AGNR.

More significant deviations, on the order of 0.08 eV for 5AGNR, are recorded in the neighborhood of the Γ point. In particular the first VB and CB have a maximum GGA-LDA discrepancy of 0.050 eV for 5AGNR and 0.045 eV for 11AGNR, which justifies the diverse band gap predictions of the two approximations (∼0.45 eV with the LDA vs ∼0.55 eV with the GGA). In this context, it is worthwhile to notice that the LDA optimization on 5AGNR, presented here, *improves* the results of a previous study [21] where a slightly smaller LDA optimized band gap of ∼0.41 eV was adopted.

Similarly, the differences of the nonoptimized and optimized band structures are small, i.e., below 0.1 eV, in an energy window of ±1.5 eV relative to the Fermi energy, as detailed in Fig. 1.

The comparison of the optimized and nonoptimized band structures of Figs. 1 and 22, in combination with the optimized atomic positions of Figs. 21 and 22, emphasize the significant role played by the GNR edges in determining the band gap. Indeed, many-body *GW* calculations produce even more marked changes [31], though, as mentioned in the main text, the GNR-substrate interaction may somehow cancel these effects [37].
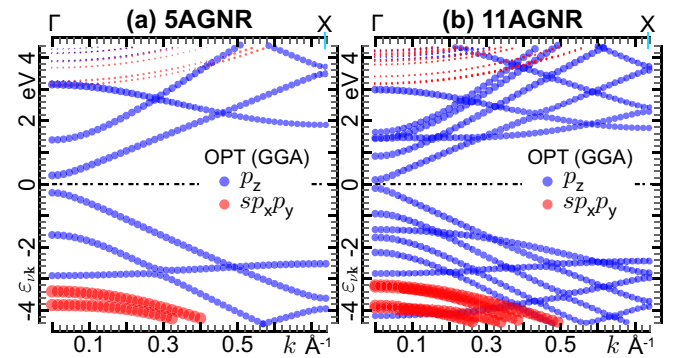
APPENDIX D: PROJECTED BAND STRUCTURE

To better clarify the nature of the intraband and interband plasmons of the GNR arrays, we report on the GGA band structure of Figs. 1 and 22, projected onto atomic orbitals of the s, p, and d type.

As shown in Fig. 23, the collective oscillations in the energy-momentum region of interest for the present study, i.e., $\hbar\omega \lesssim 2$ eV and $q \lesssim 0.2$ Å^{-1}, are associated with interband and intraband one-electron transitions coupling band states of p_z symmetry, with z denoting the outward direction to the plane of the GNR arrays. Therefore, the interband and intraband plasmons of 5AGNR and 11AGNR originate from coherent collective oscillations of π and π^* electrons, with the IntraP mode being the counterpart of the 2D plasmon of graphene.

Other interband oscillations of π-π^* nature are possible [21], at energies $\hbar\omega \sim 2$–3 eV, in 5AGNR, and $\hbar\omega \sim 1$–2.5 eV, in 11AGNR, resembling the lowest intrinsic oscillation in graphene. In addition, π-σ^* or σ-π^* oscillations are expected at energies $\hbar\omega \gtrsim 3$ eV, in 5AGNR, and $\hbar\omega \gtrsim 2.5$ eV, in 11AGNR.

APPENDIX E: INTRINSIC INTRABAND MODE

In this Appendix, we briefly report on the *thermal activation* of the intraband plasmon in intrinsic GNRs. Due to the presence of a band gap, such an oscillation is strictly absent at zero temperature.

Otherwise, the fraction of CB electrons (or VB holes) increases with increasing the working temperature, depending on the band gap value and the density of levels associated with the first CB (or first VB).

Accordingly, the IntraP loss peak is shifted to higher energy, while its intensity increases, becoming competitive with the InterP loss peak. This observation is demonstrated by the examples of Fig. 24, where a positive thermal doping was simulated, in a range of temperatures T between 0 and 2000 K. The transferred momentum was fixed to the lowest possible (longitudinal) value allowed by the MP sampling of the eV region (Appendix A 2).
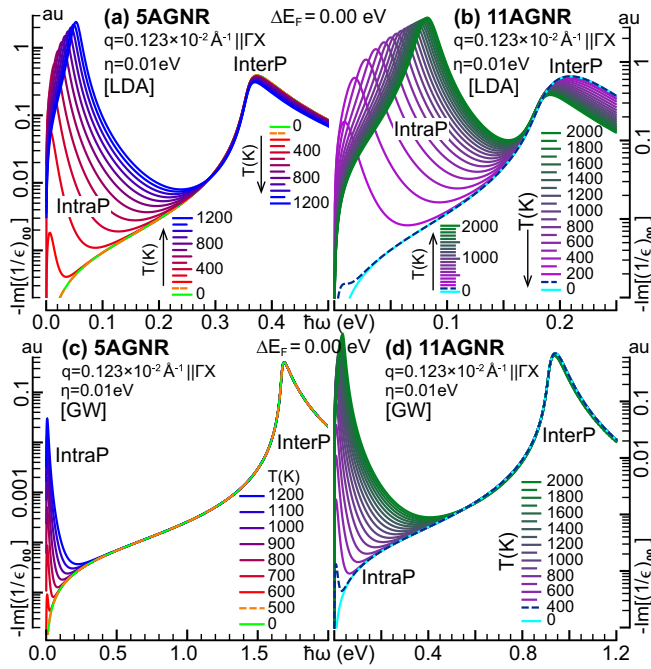
FIG. 24. Intrinsic loss function E_{LOSS} of 5AGNR [(a), (c)] and 11AGNR [(b), (d)] vs $\hbar\omega$ ranging in the energy region of the IntraP and InterP modes, with the LDA [(a), (b)] and *GW*-corrected [(c), (d)] electronic structures (Sec. II, Appendix A 1). The different plasmon spectra have been acquired at a longitudinal wave vector of 0.123×10^{-2} Å and a working temperature between 0 and 2000 K.

With the small LDA band gaps, a clear IntraP mode is detected at $T \gtrsim 200$ K in 5AGNR [Fig. 24(a)], and at $T \gtrsim 100$ K in 11AGNR [Fig. 24(b)]. On the other hand, with the *GW* band gaps, the IntraP peak is visible at $T \gtrsim 600$ K in 5AGNR [Fig. 24(c)], and $T \gtrsim 400$ K in 11AGNR [Fig. 24(d)].

Most importantly, the chosen temperatures are associated in all cases with charge carrier concentrations $n_+ < 2 \times 10^{12}$ cm^2. The latter are not sufficient to produce any Fermi level shifting above $\Delta E_G/2$, with the intrinsic Fermi energy set to zero. Indeed, the threshold concentration for positive charge carrier doping is $n_+ \sim 2.5 \times 10^{12}$ cm^2 for 5AGNR and $n_+ \sim 1.5 \times 10^{12}$ cm^2 for 11AGNR, which produce a doping level $\Delta E_F = \Delta E_G/2$ [Fig. 3(b)].

Nonetheless, the IntraP mode can be more intense than the InterP mode, say, at $T \gtrsim 500$ K in 5AGNR, with the LDA band gap [Fig. 24(a)], and 11AGNR, with both the LDA and *GW*-corrected band gaps [Figs. 24(b), 24(d)]. The InterP loss peak, however, increases in intensity with increasing the longitudinal momentum, whereas the IntraP loss peak becomes progressively weaker, as shown in Fig. 2 of the main text.

APPENDIX F: EXTRINSIC DOPING VERSUS CHARGE CARRIER SIGN

We come to the relation of the loss features of 5AGNR and 11AGNR with reversing the sign of charge carriers, passing from electron injection (+) to electron ejection (−). Working
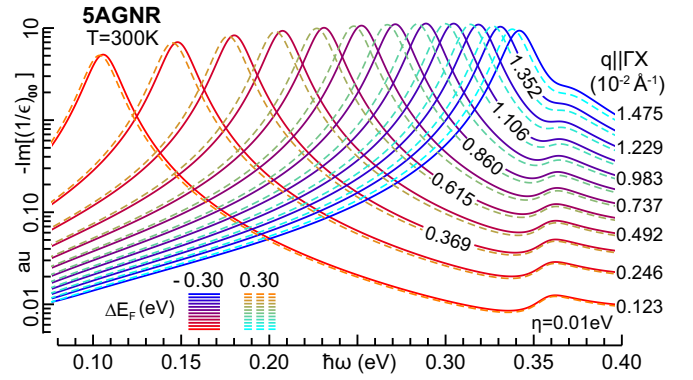

FIG. 25. Room-temperature loss function of doped 5AGNR (in atomic units), corresponding to opposite Fermi energy shifts ΔE_F of ± 0.30 eV in a range of longitudinal wave vectors $q \leqslant 0.015$ Å^{-1}.

in the LDA, we recall from Fig. 1 that the first VB and the first CB are associated with slightly different group (Fermi) velocities.

This fact has small, but non-negligible, consequences on the loss peaks of 5AGNR, for sufficiently large Fermi energy shifts and longitudinal wave vectors (Fig. 25). Conversely, the loss spectra of 11AGNR are rather insensitive to the change of doping carriers (Fig. 26).

The small asymmetry in the IntraP modes is also attested to by the different resonance frequencies at opposite charge carrier concentrations [Figs. 6(c), 6(d), 14(b), and 14(d)] and doping levels [Fig. 15(b)], occurring on both the eV and THz bands.

APPENDIX G: DIELECTRIC RESPONSE OF 29AGNR IN THE eV BAND

Now, we discuss the plasmon structure of 29AGNR in the LDA under small doping concentrations, based on an ideal unit cell, with equal bond lengths and angles, like the 5AGNR and 11AGNR unit cells of Figs. 20(c) and 21(b).

The PW-DFT step was performed as detailed in Sec. II and Appendix A 1, with the KS structure refined on a $1200 \times 1 \times$
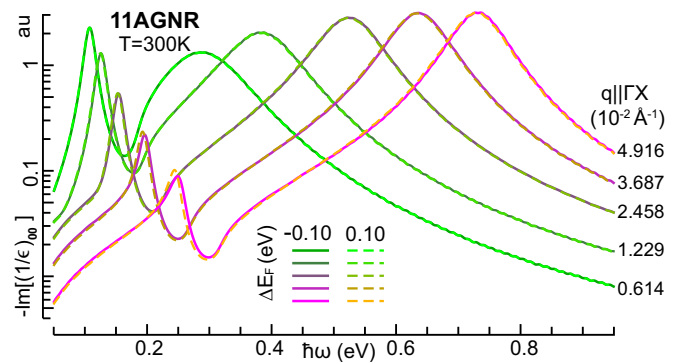

FIG. 26. Room-temperature loss function of doped 11AGNR (in atomic units), corresponding to opposite Fermi energy shifts ΔE_F of ± 0.10 eV in a range of longitudinal wave vectors $q = 0.012$–0.049 Å^{-1}.
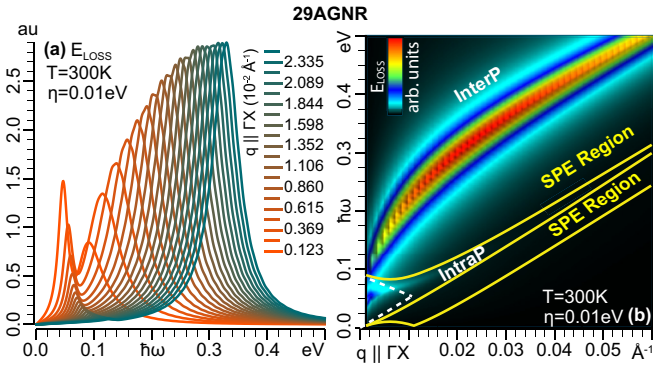
FIG. 27. Extrinsic loss function E_{LOSS} of 29AGNR vs $\hbar\omega \leqslant$ 0.5 eV, in the small (a) and large (b) momentum transfer regions, respectively, associated with longitudinal wave vectors $q < 0.0025$ Å^{-1} (a) and $q < 0.12$ Å^{-1} (b).

1 MP sampling of the first BZ, including the lowest 160 bands. Then, the TDDFT-RPA-2D scheme, leading to Eq. (4), was applied as for 5AGNR and 11AGNR.

The LDA band gap of 29AGNR turned to be 0.073 eV, and the Fermi velocities were respectively found to be $|v_+| = 0.365$ and $|v_+| = 0.380$, in Bohr velocity units, with the latter value being identical to the LDA estimate in graphene. Next, we simulated a positive charge carrier concentration of 0.8×10^{13} cm^2, equivalent to a Fermi energy shift of 0.045 eV. With these extrinsic conditions, the IntraP and InterP modes can be distinguished in the loss spectrum Fig. 27, though they appear to be strongly interacting [Fig. 27(a)].

The IntraP mode lies completely in between the two SPE regions of intraband and interband transitions [Fig. 27(b)], confirming the general features of the mode for narrower GNRs (Sec. IV). Also interesting to notice is that the no-SPE region of 29AGNR is similar to that of graphene, at small wave vectors below 0.01 Å^{-1}. We therefore expect these two regions to become more and more similar, with increasing GNR width.

APPENDIX H: LDA AND *GW* CALCULATIONS OVER THE THz BAND

We now provide some further aspects of the dielectric properties of 5AGNR and 11AGNR probed by a THz source at longitudinal wave vectors on the order of 10^4 cm^{-1}. In particular, we analyze the LDA macroscopic permittivity and the LDA and *GW* loss functions of the GNR arrays, with the same tunable parameters of Sec. V.

Accordingly, we consider (positive) charge carrier doping concentrations yielding Fermi energy shifts in the range of 0.01 to 0.14 eV, above the threshold $\Delta E_G/2$ (with the intrinsic Fermi level set to 0), and we focus on the intraband plasmon features, at frequencies below $\sim$10 THz.

Figure 28 shows the real permittivity Re(ϵ^M) as a function of the probing frequency, at a fixed transferred momentum. The IntraP mode is a genuinely undamped plasmon, associated with a couple of zeros in Re(ϵ^M), with the second zeros (intraband resonances) ω_P being negligibly smaller than the loss peak frequencies ω_L of Fig. 14.
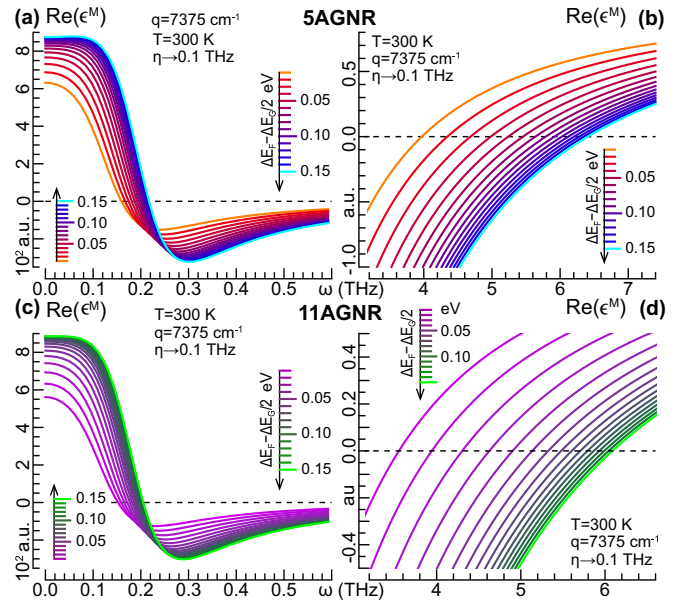

FIG. 28. Real permittivity Re(ϵ^M) of 5AGNR [(a), (b)] and 11AGNR [(c), (d)] for $\omega < 0.6$ THz [(a), (c)] and $3 < \omega < 7$ THz [(b), (d)] at room temperature, with the lowest sampled wave vector of the THz calculations (Sec. V) and doping levels inducing Fermi energy shifts in the range of 0.01–0.14 eV, relative to the threshold for positive charge carrier doping.

Figure 29 shows the loss function of the systems in the same frequency range. It can be observed that E_{LOSS} is independent of the band gap on the lower THz domain, where the intraband plasmon is located.

Indeed, both the LDA and *GW*-corrected electronic structures produce the same plasmon spectra for $\omega < 50$ THz [in 5AGNR, Fig. 29(a)] and $\omega < 25$ THz [in 5AGNR, Fig. 29(b)]. Accordingly the IntraP mode on the THz band is excellently described by the TDDFT-RPA-2D framework developed here,
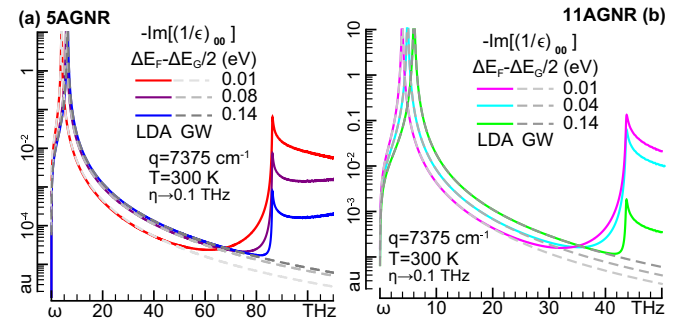

FIG. 29. Loss spectra E_{LOSS} of 5AGNR (a) and 11AGNR (b), computed with the LDA and *GW*-corrected band structures, for $\omega < 110$ THz (a) and $\omega < 50$ THz (b). All other settings are as in Fig. 28. The LDA curves show also the contribution of the InterP mode, occurring at $\sim$86 THz in 5AGNR and $\sim$44 THz in 11AGNR. With *GW* calculations, the same peak is shifted (and not shown) to $\sim$404 THz in 5AGNR and $\sim$220 THz in 11AGNR.

within the LDA band structure, which is supported by a number of available efficient DFT-PW packages.

APPENDIX I: DIELECTRIC RESPONSE IN THE VANISHING MOMENTUM LIMIT

As a last Appendix, we take advantage of the analytical model of Sec. VI to explore the $q \to 0$ behavior of the permittivity of the GNR arrays. Starting from Eq. (8), we may perform a power series expansion of the different terms included in the unperturbed susceptibility of Eq. (6), namely, the band energies of Eq. (1), occupation factors, and correlation terms of Eq. (7e). Then, we get the limiting expression

$$\epsilon_{\text{NLF}}^{\text{M}} \approx \epsilon_0 - \frac{2q\cos^2\theta}{\pi(\hbar\omega + i\eta)^2} \int_{-k_{\Gamma X}}^{k_{\Gamma X}} dk (f'_{1k}\varepsilon'_{1k} + f'_{-1k}\varepsilon'_{-1k})$$
$$- \frac{4q\cos^2\theta}{L_y} \int_{-k_{\Gamma X}}^{k_{\Gamma X}} \frac{dk}{Q(k)^2} \frac{(f_{1k} - f_{-1k})(\varepsilon_{1k} - \varepsilon_{-1k})}{(\varepsilon_{-1k} - \varepsilon_{1k})^2 + (\hbar\omega + i\eta)^2}$$
$$+ o(q^2), \tag{I1}$$

where $\varepsilon'_{\pm 1k} = \partial\varepsilon_{\pm 1k}/\partial k$, $f'_{\pm 1k} = \partial f_{\pm 1k}/\partial k$. This form correctly tends to the static vacuum permittivity with q tending to zero, or θ approaching the transverse direction to the GNR axis.

[1] R. F. Oulton, V. J. Sorger, T. Zentgraf, R.-M. Ma, C. Gladden, L. Dai, G. Bartal, and X. Zhang, Plasmon lasers at deep subwavelength scale, Nature (London) **461**, 629 (2009).

[2] R. Jiang, B. Li, C. Fang, and J. Wang, Metal-semiconductor hybrid nanostructures for plasmon-enhanced applications, Adv. Mater. **26**, 5274 (2014).

[3] A. K. Geim and K. S. Novoselov, The rise of graphene, Nat. Mater. **6**, 183 (2007).

[4] A. H. Castro Neto, F. Guinea, N. M. R. Peres, K. S. Novoselov, and A. K. Geim, The electronic properties of graphene, Rev. Mod. Phys. **81**, 109 (2009).

[5] L. Ju, B. Geng, J. Horng, C. Girit, M. Martin, Z. Hao, H. A. Bechtel, X. Liang, A. Zettl, Y. R. Shen *et al.*, Graphene plasmonics for tunable terahertz metamaterials, Nat. Nanotechnol. **6**, 630 (2011).

[6] A. N. Grigorenko, M. Polini, and K. S. Novoselov, Graphene plasmonics, Nat. Photonics **6**, 749 (2012).

[7] J. Christensen, A. Manjavacas, S. Thongrattanasiri, F. H. L. Koppens, and F. J. García de Abajo, Graphene plasmon waveguiding and hybridization in individual and paired nanoribbons, ACS Nano **6**, 431 (2012).

[8] N. J. Halas, S. Lal, W.-S. Chang, S. Link, and P. Nordlander, Plasmons in strongly coupled metallic nanostructures, Chem. Rev. **111**, 3913 (2011).

[9] M. Xu, T. Liang, M. Shi, and H. Chen, Graphene-like two-dimensional materials, Chem. Rev. **113**, 3766 (2013).

[10] X.-Z. Yan, Y. Romiah, and C. S. Ting, Electric transport theory of Dirac fermions in graphene, Phys. Rev. B **77**, 125409 (2008).

[11] L. A. Falkovsky, Optical properties of graphene, J. Phys.: Conf. Ser. **129**, 012004 (2008).

[12] S. Thongrattanasiri, A. Manjavacas, and J. F. García de Abajo, Quantum finite-size effects in graphene plasmons, ACS Nano **6**, 1766 (2012).

[13] F. J. García de Abajo, Graphene plasmonics: Challenges and opportunities, ACS Photonics **1**, 135 (2014).

[14] D. Mencarelli, S. Bellucci, A. Sindona, and L. Pierantoni, Spatial dispersion effects upon local excitation of extrinsic plasmons in a graphene micro-disk, J. Phys. D: Appl. Phys. **48**, 465104 (2015).

[15] H. Lu, C. Zeng, Q. Zhang, X. Liu, M. M. Hossain, P. Reineck, and M. Gu, Graphene-based active slow surface plasmon polaritons, Sci. Rep. **5**, 8443 (2015).

[16] S. Zhong, Y. Lu, C. Li, H. Xu, F. Shi, and Y. Chen, Tunable plasmon lensing in graphene-based structure exhibiting negative refraction, Sci. Rep. **7**, 41788 (2017).

[17] P. Avouris, T. F. Heinz, and T. Low (eds.), *2D Materials: Properties and Devices* (Cambridge University Press, Cambridge, UK, 2017).

[18] M. Ota, A. Sumimura, M. Fukuhara, Y. Ishii, and M. Fukuda, Plasmonic-multimode-interference-based logic circuit with simple phase adjustment, Sci. Rep. **6**, 24546 (2016).

[19] C. Vacacela Gomez, M. Guevara, T. Tene, L. S. Lechon, B. Merino, H. Brito, and S. Bellucci, Energy gap in graphene and silicene nanoribbons: A semiclassical approach, in *Proceedings of the Second International Congress on Physics Espoch (ICPE-2017)*, edited by C. L. Vásconez, AIP Conf. Proc. 2003 (AIP, New York, 2018), p. 020015.

[20] X. Liu, J. B. Oostinga, A. F. Morpurgo, and L. M. K. Vandersypen, Electrostatic confinement of electrons in graphene nanoribbons, Phys. Rev. B **80**, 121407(R) (2009).

[21] C. Vacacela Gomez, M. Pisarra, M. Gravina, J. M. Pitarke, and A. Sindona, Plasmon Modes of Graphene Nanoribbons with Periodic Planar Arrangements, Phys. Rev. Lett. **117**, 116801 (2016).

[22] C. Vacacela Gomez, M. Pisarra, M. Gravina, and A. Sindona, Tunable plasmons in regular planar arrays of graphene nanoribbons with armchair and zigzag-shaped edges, Beilstein J. Nanotechnol. **8**, 172 (2017).

[23] T. Eberlein, U. Bangert, R. R. Nair, R. Jones, M. Gass, A. L. Bleloch, K. S. Novoselov, A. Geim, and P. R. Briddon, Plasmon spectroscopy of free-standing graphene films, Phys. Rev. B **77**, 233406 (2008).

[24] M. Pisarra, A. Sindona, P. Riccardi, V. M. Silkin, and J. M. Pitarke, Acoustic plasmons in extrinsic free-standing graphene, New J. Phys. **16**, 083003 (2014).

[25] N. K. Emani, D. Wang, T.-F. Chung, L. J. Prokopeva, A. V Kildishev, V. M. Shalaev, Y. P. Chen, and A. Boltasseva, Plasmon resonance in multilayer graphene nanoribbons, Laser Photonics Rev. **9**, 650 (2015).

[26] W. Wang, P. Apell, and J. Kinaret, Edge plasmons in graphene nanostructures, Phys. Rev. B **84**, 085423 (2011).

[27] Z. Fei, M. D. Goldflam, J.-S. Wu, S. Dai, M. Wagner, A. S. McLeod, M. K. Liu, K. W. Post, S. Zhu, G. C. A. M. Janssen, M. M. Fogler, and D. N. Basov, Edge and surface plasmons in graphene nanoribbons, Nano Lett. **15**, 8271 (2015).

[28] H. Hou, J. Teng, T. Palacios, and S. Chua, Edge plasmons and cut-off behavior of graphene nano-ribbon waveguides, Opt. Commun. **370**, 226 (2016).

[29] C. Lu, J. Wang, S. Yan, Z.-D. Hu, G. Zheng, and L. Yang, Tunable multiple plasmon-induced transparencies based on

asymmetrical grapheme nanoribbon structures, Materials **10**, 699 (2017).

[30] Y.-W. Son, M. L. Cohen, and S. G. Louie, Energy Gaps in Graphene Nanoribbons, Phys. Rev. Lett. **97**, 216803 (2006).

[31] L. Yang, C.-H. Park, Y.-W. Son, M. L. Cohen, and S. G. Louie, Quasiparticle Energies and Band Gaps in Graphene Nanoribbons, Phys. Rev. Lett. **99**, 186801 (2007).

[32] V. V. Popov, T. Y. Bagaeva, T. Otsuji, and V. Ryzhii, Oblique terahertz plasmons in graphene nanoribbon arrays, Phys. Rev. B **81**, 073404 (2010).

[33] D. R. Andersen and H. Raza, Plasmon dispersion in semimetallic armchair graphene nanoribbons, Phys. Rev. B **85**, 075425 (2012).

[34] A. Kimouche, M. M. Ervasti, R. Drost, S. Halonen, A. Harju, P. M. Joensuu, J. Sainio, and P. Liljeroth, Ultra-narrow metallic armchair graphene nanoribbons, Nat. Commun. **6**, 10177 (2015).

[35] L. Talirz, H. Söde, T. Dumslaff, S. Wang, J. R. Sanchez-Valencia, J. Liu, P. Shinde, C. A. Pignedoli, L. Liang, V. Meunier *et al.*, On-surface synthesis and characterization of 9-atom wide armchair graphene nanoribbons, ACS Nano **11**, 1380 (2017).

[36] J. P. Llinas, A. Fairbrother, G. B. Barin, W. Shi, K. Lee, S. Wu, B. Y. Choi, R. Braganza, J. Lear, N. Kau *et al.*, Short-channel field-effect transistors with 9-atom and 13-atom wide graphene nanoribbons, Nat. Commun. **8**, 633 (2017).

[37] W.-X. Wang, M. Zhou, X. Li, S.-Y. Li, X. Wu, W. Duan, and L. He, Energy gaps of atomically precise armchair graphene sidewall nanoribbons, Phys. Rev. B **93**, 241403(R) (2016).

[38] M. Petersilka, U. J. Gossmann, and E. K. U. Gross, Excitation Energies from Time-Dependent Density-Functional Theory, Phys. Rev. Lett. **76**, 1212 (1996).

[39] G. Onida, L. Reining, and A. Rubio, Electronic excitations: Density-functional versus many-body Green's-function approaches, Rev. Mod. Phys. **74**, 601 (2002).

[40] W. Kohn and L. J. Sham, Self-consistent equations including exchange and correlation effects, Phys. Rev. **140**, A1133 (1965).

[41] J. P. Perdew and A. Zunger, Self-interaction correction to density-functional approximations for many-electron systems, Phys. Rev. B **23**, 5048 (1981).

[42] J. P. Perdew, K. Burke, and M. Ernzerhof, Generalized Gradient Approximation Made Simple, Phys. Rev. Lett. **77**, 3865 (1996).

[43] N. Troullier and J. L. Martins, Efficient pseudopotentials for plane-wave calculations, Phys. Rev. B **43**, 1993 (1991).

[44] D. R. Hamann, Optimized norm-conserving Vanderbilt pseudopotentials, Phys. Rev. B **88**, 085117 (2013).

[45] Z. H. Levine and D. C. Allan, Linear Optical Response in Silicon and Germanium Including Self-Energy Effects, Phys. Rev. Lett. **63**, 1719 (1989).

[46] A. Sindona, M. Pisarra, C. Vacacela Gomez, P. Riccardi, G. Falcone, and S. Bellucci, Calibration of the fine-structure constant of graphene by time-dependent density-functional theory, Phys. Rev. B **96**, 201408(R) (2017).

[47] V. Barone, O. Hod, and G. E. Scuseria, Electronic structure and stability of semiconducting graphene nanoribbons, Nano Lett. **6**, 2748 (2006).

[48] S. L. Adler, Quantum theory of the dielectric constant in real solids, Phys. Rev. **126**, 413 (1962).

[49] N. Wiser, Dielectric constant with local field effects included, Phys. Rev. **129**, 62 (1963).

[50] V. Despoja, D. J. Mowbray, D. Vlahović, and L. Marušić, TDDFT study of time-dependent and static screening in graphene, Phys. Rev. B **86**, 195429 (2012).

[51] A. Sindona, A. Cupolillo, F. Alessandro, M. Pisarra, D. C. Coello Fiallos, S. M. Osman, and L. S. Caputi, Interband π-like plasmon in silicene grown on silver, Phys. Rev. B **97**, 041401(R) (2018).

[52] Here, we should point out that the converted values of $n_\pm$ to ΔE_F in 5AGNR [Fig. 3(b)] differ from those reported in a previous study [21], where the LDA calculations were performed on a geometry-optimized unit cell, with a slightly larger band gap of ∼0.41 eV.

[53] D. B. Farmer, R. Golizadeh-Mojarad, V. Perebeinos, Y.-M. Lin, G. S. Tulevski, J. C. Tsang, and P. Avouris, Chemical doping and electron-hole conduction asymmetry in graphene devices, Nano Lett. **9**, 388 (2008).

[54] A. Das, S. Pisana, B. Chakraborty, S. Piscanec, S. K. Saha, U. V. Waghmare, K. S. Novoselov, H. R. Krishnamurthy, A. K. Geim, A. C. Ferrari *et al.*, Monitoring dopants by Raman scattering in an electrochemically top-gated graphene transistor, Nat. Nanotechnol. **3**, 210 (2008).

[55] E. H. Hwang and S. Das Sarma, Dielectric function, screening, and plasmons in two-dimensional graphene, Phys. Rev. B **75**, 205418 (2007).

[56] G. Strinati, H. J. Mattausch, and W. Hanke, Dynamical aspects of correlation corrections in a covalent crystal, Phys. Rev. B **25**, 2867 (1982).

[57] C. Kramberger, R. Hambach, C. Giorgetti, M. H. Rümmeli, M. Knupfer, J. Fink, B. Büchner, Lucia Reining, E. Einarsson, S. Maruyama, F. Sottile, K. Hannewald, V. Olevano, A. G. Marinopoulos, and T. Pichler, Linear Plasmon Dispersion in Single-Wall Carbon Nanotubes and the Collective Excitation Spectrum of Graphene, Phys. Rev. Lett. **100**, 196803 (2008).

[58] A. Sindona, M. Pisarra, D. Mencarelli, L. Pierantoni, and S. Bellucci, Plasmon modes in extrinsic graphene: *Ab initio* simulations vs semi-classical models, *Fundamental and Applied Nano-Electromagnetics* (Springer Netherlands, Dordrecht, 2016), pp. 125–144.

[59] X. Gonze, F. Jollet, F. Abreu Araujo, D. Adams, B. Amadon, T. Applencourt, C. Audouze, J.-M. Beuken, J. Bieder, A. Bokhanchuk *et al.*, Recent developments in the ABINIT software package, Comput. Phys. Commun. **205**, 106 (2016).

[60] H. J. Monkhorst and J. D. Pack, Special points for Brillouin-zone integrations, Phys. Rev. B **13**, 5188 (1976).

[61] G. Kresse and J. Hafner, *Ab initio* molecular dynamics for liquid metals, Phys. Rev. B **47**, 558 (1993).

[62] M. Pisarra, A. Sindona, M. Gravina, V. M. Silkin, and J. M. Pitarke, Dielectric screening and plasmon resonances in bilayer graphene, Phys. Rev. B **93**, 035440 (2016).

[63] M. Pisarra, P. Riccardi, A. Sindona, A. Cupolillo, N. Ligato, C. Giallombardo, and L. Caputi, Probing graphene interfaces with secondary electrons, Carbon **77**, 796 (2014).